20

BEAM POWER ABSORPTION DEVICES

A. H. Kilert, L. R. Lucas, W. S. Scott, and D. R. Walz, Editor

The ever-increasing energy and beam intensity of particle accelerators and the resulting high-power densities pose some challenging problems. One such problem is the successful absorption and dissipation of the power from a particle beam incident on matter. The SLAC beam switchyard (BSY) contains two beam transport systems to momentum-analyze the electron beam and to deflect it into physically separated research areas. In the course of traversing the BSY, the electron beam could impinge on many transport system components, such as magnets, beam position and profile monitors, current monitors, vacuum chambers, and targets for production of secondary particle beams. All but the last of these components are not designed for power dissipation and might suffer serious damage or total destruction if exposed to the high-power density beam. High-energy physics experiments often require a precise determination of the beam momentum and acceptance of a narrow momentum band. The bending magnets of the beam transport system serve to analyze the momentum of the beam. This analysis, in turn, allows removal of particles outside of the acceptable momentum band. Thus, devices which can absorb and safely dissipate rather high-power densities are required. Finally, the remaining electron beam leaving a target must be disposed of.

This chapter presents a summary of the research, development, design, and fabrication of beam power absorption devices. The first section treats beam interactions with materials, starting with the electromagnetic cascade shower development, and followed by the resulting power deposition and temperature rise. The pertinent modes of heat transfer are briefly reviewed, and auxiliary problems such as thermal stress and thermal fatigue are dealt with. In the following two sections, high-power and low-power beam dumps for continuous absorption and dissipation of up to 2.2 MW average beam power are discussed and analyzed. Radiolysis and radioactivity in the

cooling-water systems are treated in some detail with the inclusion of experimental results. Then, variable-aperture high-power and low-power slits and collimators are discussed and their final versions and first performance data are presented and illustrated with photographs. The treatment is supplemented by a slit analysis including a numerical example. Next follows a section on protection collimators with emphasis on protection philosophy, beam trajectory, and beam envelope studies. Finally, a few thoughts on future high-power absorption devices are offered. It is hoped that this chapter, in addition to presenting the high-power absorbers as built at SLAC, will serve as a guide for development of such devices at other laboratories. A list of pertinent references completes the chapter.

20-1 Beam interactions with materials (DRW)

The following treatment summarizes the most important phenomena to be considered in the development of high-power absorbing equipment. Electromagnetic cascade shower development, power deposition and temperature rise, heat transfer, thermal stress development, thermal fatigue, and thermal shock are reviewed. The list does not claim to be complete and a number of other important topics such as radiation levels and radiation damage, radiolysis and induced radioactivity, metallurgy and corrosion problems are dealt with using specific examples in the sections below.

Cascade shower development

High-energy electrons such as those produced by the SLAC linac will gradually lose their energy upon traversing matter. This energy is lost primarily as a consequence of electromagnetic interactions in the form of radiation effects and collisions with atomic electrons. Extensive literature[1] exists, and only the most important processes are dealt with here.

The important processes for electrons are radiation or bremsstrahlung and ionization; for photons, pair production and Compton scattering. A multigigaelectron-volt electron beam impinging on matter will cause production of a large number of secondary particles.

Upon traversing the electric field of nuclei, electrons are deflected and radiate photons. This process is referred to either as radiation or as bremsstrahlung. It can occur many times for incident 20-GeV electrons, and the total secondary particle population rises rapidly as a function of depth. As the energy of the electrons decreases the probability of a radiation interaction decreases also, whereas the probability for "absorption" and associated "ionization" increases.

The photons produced in the bremsstrahlung process can have various interactions with matter depending on their energy. A high-energy photon produced by an incident electron will most likely interact with the nucleus in a process in which the photon disappears and two new particles, an electron

and a positron, are released. The energy of the photon appears primarily as kinetic energy of the electron and positron. The process is called "pair production." Both secondary particles are still highly energetic and can liberate more photons by bremsstrahlung. These photons, in turn, can materialize in pair production. Thus, the population of electrons, photons, and positrons increases rapidly at the expense of the average energy of the particles. This phenomenon is called the development of an "electromagnetic cascade shower."

After traversing a certain amount of matter, the particle population reaches a maximum which is referred to as the shower maximum. This is also the location of peak energy deposition in matter, as this quantity is proportional to the shower multiplicity.

As the energy of the photons decreases to the range of 1 to 5 MeV, they interact mainly by elastic scattering with the orbital electrons of the atom; the photon is scattered and the electrons recoil. After several elastic scattering collisions the photon has lost much energy and the probability of its being absorbed in a collision with an atomic electron is greatly increased. When this happens, an electron is ejected from the atom and the photon disappears. This phenomenon is referred to as "photoelectric absorption." Thus, as the radiation shower traverses beyond the shower maximum, the total number of electrons, positrons, and photons decreases; the shower is exponentially attenuated.

Equations to compute the total number of electrons or photons in a shower due to an incident electron or photon, respectively, have been given.[1] At the shower maximum, the number of electrons, $\Pi_{\max}^{(e^-)}$, due to an incident electron of energy E_0 is

$$\Pi_{\max}^{(e^-)} = 0.31\left(\frac{E_0}{\varepsilon_0}\right)\left[\ln\left(\frac{E_0}{\varepsilon_0}\right) - 0.37\right]^{-1/2} \tag{20-1}$$

and the number of photons, $\Pi_{\max}^{(\gamma)}$, due to an incident photon of energy E_0 is

$$\Pi_{\max}^{(\gamma)} = 0.31\left(\frac{E_0}{\varepsilon_0}\right)\left[\ln\left(\frac{E_0}{\varepsilon_0}\right) - 0.18\right]^{-1/2} \tag{20-2}$$

where ε_0 is the critical energy of the target material, i.e., the average energy loss due to ionization (or radiation), per unit radiation length.

The longitudinal distance in radiation lengths to the shower maximum can be computed from

$$T_{\max}^{(e^-)} = 1.01\left[\ln\left(\frac{E_0}{\varepsilon_0}\right) - 1\right] \tag{20-3}$$

and

$$T_{\max}^{(\gamma)} = 1.01\left[\ln\left(\frac{E_0}{\varepsilon_0}\right) - 0.5\right] \tag{20-4}$$

where one radiation length, X_0, is defined as the distance (of matter traversed) in which an electron's energy is reduced by radiation to $1/e$ of its original value. The radiation shower develops not only in the direction of the incident electron beam but also radially. At the beginning of the shower, where the average energy of the particles is still high, scattering angles of the shower particles are small, and secondary electrons, positrons, and photons are also emitted at small angles. Thus, the shower develops mainly in the forward or longitudinal direction. As the average energy of the shower particles decreases, scattering and emission angles become larger, and a significant radial shower development results. This has a profound influence on lateral dimensions of energy-absorbing equipment.

Evaluation of cascade showers is a very difficult mathematical task. Approximations and simplifications have to be introduced to make calculations practical. Relatively few simplifications are made in Monte Carlo calculations, using differential and total cross sections for the various processes described above. The longitudinal shower development has been treated in detail analytically.[1] More recently a Monte Carlo method to calculate the three-dimensional shower has been developed.[2,3] This method was used to study the effectiveness of an aluminum collimator in a 20-GeV electron beam.[4] The results are based on a single incident electron, i.e., a point source; they are thus not particularly useful for practical applications. Assumption of a point source results in unrealistically high energy densities near the origin.

Figure 20-1 Longitudinal shower development of a 20-GeV, 2.18-MW electron beam in water, aluminum, and copper.

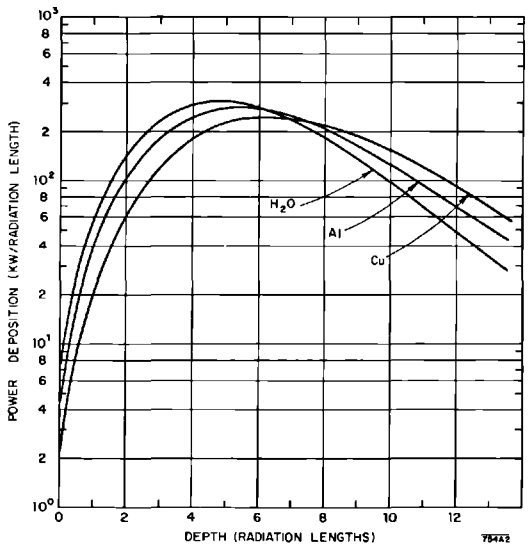

Point source results of the three-dimensional shower in semi-infinite media of copper, aluminum, and water have been transformed into physically realizable finite-sized beams assuming a Gaussian radial beam distribution.[5] Three different incident beam profiles having standard deviations of $\sigma_b = 0.1$, 0.3, and 1.0 cm were treated. All values are for radially symmetric, 20-GeV, incident electron beams with a repetition rate of 360 pulses/sec, a pulse length of 2.1×10^{-6} sec, and an average beam power of 2.18 MW. These beam data allow conversion of the energy densities obtained in the Monte Carlo calculations into power densities. The longitudinal power deposition in Cu, Al, and H_2O is shown in Fig. 20-1. The curves are for $\sigma_b = 0.3$ cm, a beam size closely resembling expected operating conditions. Figure 20-2 presents the corresponding radial power distribution at the shower maximum.

Power deposition and temperature rise

A close examination of the relationships given in Figs. 20-1 and 20-2 reveals some interesting facts. The energy deposition rates at the shower maximum and at the origin, $r = 0$, are very high. Using radiation length values from Table 20-1, volume heat sources of $S = 198$, 16.4, and 2.2 kW/cm^3 for copper, aluminum, and water, respectively, can be computed. The resulting local temperature rise, ΔT, assuming uniform heat source distribution in the volume

Figure 20-2 Radial shower development of a 20-GeV, 2.18-MW electron beam at the shower maximum (for $\sigma_b = 0.3$ cm) in water, aluminum, and copper.

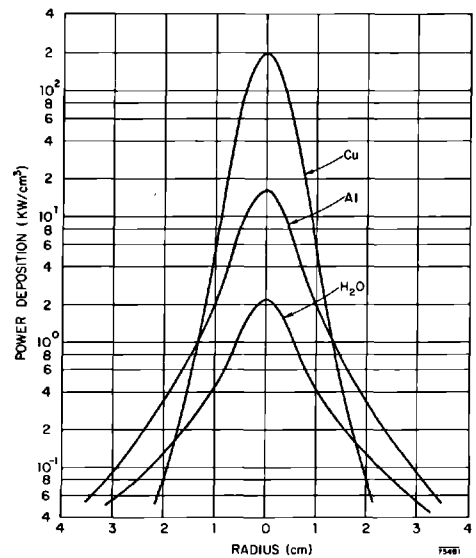

element under consideration, is spectacular. It can readily be calculated from

$$\Delta T = \frac{S}{\rho c(\mathrm{PRR})} \tag{20-5}$$

where S is the heat source from Fig. 20-2 in watts per cubic centimeter, ρ and c are the specific gravity and specific heat of the material in grams per cubic centimeter and watt-seconds per gram-degree centigrade, respectively, PRR is the pulse repetition rate in pulses per second, and ΔT is in degrees centigrade per pulse. For the heat source values at $r = 0$, as presented above, Eq. (20-5) gives for copper $\Delta T_{\max} = 158°\mathrm{C/pulse}$, for aluminum 18°C/pulse, and for water 1.5°C/pulse.

Maximum power densities and calculated peak temperature rises per pulse have been presented[6] and an abstract is given in Table 20-1 for two standard deviations, $\sigma_b = 0.1$ cm and $\sigma_b = 0.3$ cm. For other materials, the maximum power deposition can be determined from

$$S = \frac{\Pi_{\max} P_{\mathrm{AV}} \rho}{AE_0} \frac{dE}{dx} \tag{20-6}$$

where $\Pi_{\max}$ can be evaluated from either Eq. (20-1) or Eq. (20-2), P_{AV} is the average incident beam power, E_0 is the energy of the incident beam, A is the beam-spread area at shower maximum, and $dE/dx = \varepsilon_0/X_0$ is the energy loss of the shower electrons. A number of potentially useful materials for energy absorber applications, including important material constants, have been given.[6] An expanded, slightly altered version is presented in Table 20-2. Calculated values are based on $E_0 = 20$ GeV, $P_{\mathrm{AV}} = 2.2$ MW, and $A = 1\ \mathrm{cm}^2$.

Table 20-1 Maximum power densities and peak temperature rises at the shower maximum in copper, aluminum, and water[a]

	Depth		*$\sigma_b = 0.1$ cm*		*$\sigma_b = 0.3$ cm*	
Material	*Radiation lengths*	*cm*	*S (kW/cm³)*	*ΔT (°C/pulse)*	*S (kW/cm³)*	*ΔT (°C/pulse)*
Cu	0.0– 0.5	0.0 – 0.716	57.2	45.1	6.6	5.2
	6.0– 6.5	8.59– 9.31	920.0	725.5	198.1	156.2
	9.5–10.0	13.60– 14.32	328.8	259.3	86.1	67.9
Al	0.0– 0.5	0.0 – 4.52	14.4	15.7	1.9	2.1
	5.0– 5.5	45.2 – 49.7	56.6	61.7	16.4	17.9
	9.5–10.0	85.8 – 90.3	14.2	15.5	4.4	4.8
H_2O	0.0– 0.5	0.0 – 18.65	4.5	3.0	0.73	0.5
	4.5– 5.0	167.8 –186.5	7.1	4.7	2.2	1.5
	9.5–10.0	354.3 –373.0	1.0	0.7	0.33	0.22

[a] For $E_0 = 20$ GeV, $P_{\mathrm{AV}} = 2.18$ MW.

Table 20-2 **Properties and characteristics of potentially useful materials for energy absorber applications**[a]

Characteristics		Materials									
		Be	*C Pyrolytic*	*H_2O*	*Al*	*Ti*	*Fe*	*Cu*	*Ta*	*W*	*Pb*
Z		4	6	7.23	13	22	26	29	73	74	82
ε_0[b,c]	(MeV)	110.0	79.0	72.8	40.0	24.0	20.6	18.8	8.2	8.1	7.4
X_0[b]	(g/cm²)	66.0	43.3	35.7	24.3	15.1	13.9	13.0	6.9	6.8	6.5
$T_{\max}^{(e^-)}$	(radiation-lengths)	4.24	4.57	4.66	5.28	5.80	5.93	6.06	6.85	6.86	6.98
$\Pi_{\max}^{e^-}$		25.6	34.5	37.0	64.0	103.0	118.0	131.0	277.0	281.0	305.0
$-\frac{dE}{dx}$	(MeV/(g/cm²)	1.67	1.82	2.03	1.64	1.59	1.48	1.44	1.19	1.18	1.14
ρ	(g/cm³)	1.85	2.0	1.0	2.70	4.50	7.87	8.95	16.6	19.3	11.35
$-\rho\frac{dE}{dx}$	(MeV/cm)	3.08	3.64	2.03	4.45	7.17	11.6	12.8	19.8	22.7	12.9
c	(W-sec/g-°C)	1.78	0.97	4.22	0.94	0.54	0.48	0.385	0.129	0.134	0.13
ρc	(W-sec/cm³-°C)	3.3	1.94	4.22	2.54	2.42	3.79	3.45	2.14	2.58	1.48
k	$\left(\frac{\text{W}}{\text{cm}^2\text{-°C/cm}}\right)$	1.68	0.025 2.0	0.006	2.39	0.17	0.63	3.9	0.63	1.46	0.083
T_{melt}	(°C)	1278.0	3600.0		659.0	1800.0	1530.0	1083.0	3000.0	3380.0	327.0
S	(kW/cm³)	8.7	13.8	8.3	31.1	81.5	152.0	186.0	601.0	696.0	431.0
ΔT	(°C/pulse)	7.3	19.7	5.5	34.1	102.0	112.0	150.0	772.0	748.0	807.0
$\alpha\cdot 10^6$	(1/°C)	12.3	$+0.06$ -0.8		25.0	8.7	12.1	16.6	6.7	4.3	29.4
$E\cdot 10^{-6}$	(psi)	44.0	4.4		10.0	15.0	29.0	17.0	27.0	51.0	2.3
αE	(psi/°C)	540.0	$+0.26$ -3.5		250.0	130.0	350.0	282.0	181.0	220.0	68.0

[a] $E_0 = 20$ GeV, $P_{AV} = 2.2$ MW, and $A = 1$ cm².
[b] Most values from O. I. Dovzhenko and A. A. Pomanskii, *J. Exptl. Theoret. Phys.* (*U.S.S.R.*) **45**, 268–278 (1963).
[c] All values take density effect into account.

It should be noted that using $A = \text{const.}$ does not adequately account for the radial shower development as a function of Z; therefore, the temperature rise and power deposition as computed from Eqs. (20-5) and (20-6) are high for low-Z materials, approximately correct for medium-Z materials, and low for high-Z materials.

The values shown in Tables 20-1 and 20-2 indicate clearly that medium- and high-Z materials are not useful for applications requiring continuous exposure to the beam. Energy is deposited at a much higher rate than can be handled by thermal diffusion for practical geometries. The local temperature increases dramatically with each successive pulse, and failure due to gross geometrical changes or melting results for most of these materials within a fraction of 1 sec. Note that the product of ρc, i.e., the specific heat capacity, is essentially constant for all metals.

Further examination of Table 20-2 indicates that low-Z materials offer some promise for successful application in the construction of energy absorbers for high power density beams. In low-Z materials the power is dissipated in a much larger volume, i.e., the heat source is less intense.

Heat transfer problems

In the previous section it was shown how to calculate rates of heat deposition and local temperature rises per pulse. The next step in the course of an energy absorber analysis is the determination of the temperature distribution resulting from the beam power deposition and boundary conditions imposed on the system. Heat transfer between two adjacent particles of matter is the transfer of thermal (heat) energy by virtue of a temperature difference from the hotter to the colder. In any solid energy absorber, heat is transferred solely by thermal conduction. In an isotropic body the law of heat conduction can be stated as

$$q'' = -k \frac{\partial T}{\partial n} \tag{20-7}$$

where q'' is the heat flux in a direction n, and k is the thermal conductivity. Using Eq. (20-7), the most general equation describing the temperature distribution in any solid can be derived. If the thermal conductivity is assumed to be constant the heat equation (Fourier's law of conduction) can be stated as

$$k\nabla^2 T + S = \rho c \frac{\partial T}{\partial \tau} \tag{20-8}$$

where ∇^2 is the Laplacian operator, S is the rate of heat generation per unit volume, and τ is the time; S may be a function of space and time. For steady-state conditions with no internal heat generation, Eq. (20-8) reduces to the familiar Laplace equation. The heat equation has been solved for a wide variety of applications.[7]

Even when low-Z materials are used, so that heat source intensities are greatly reduced, the resulting heat fluxes from a surface are very high for practical geometries. Consider the case of an aluminum slab of thickness $\delta = 0.5$ cm placed normal to the beam direction at the shower maximum. Assume that one side of the slab faces a vacuum and the other side is water cooled. To a first approximation the heat sources are uniformly distributed through the cylindrical volume defined by the thickness of the slab and the effective diameter of the incident particle beam. This volume element for a 1-cm diameter beam is 0.39 cm^3, and the volume heat source is $S \approx 12$ kW/cm^3 (from Fig. 20-2 assuming a beam of 20-GeV energy and 2.18-MW average power). The power dissipated in this space is then $P_{AV} = 4.7$ kW. Neglecting radial conduction for the time being, it is found that the resultant steady-state local heat flux in the beam direction from the slab and into the water is $q'' = 6.0$ kW/cm^2. This is a very high if not excessive heat flux. A solution to Eq. (20-8) will readily yield the temperature rise across the slab as

$$\Delta T = \frac{q''}{k}\left(\frac{\delta}{2}\right) \tag{20-9}$$

which would be approximately 630°C. Consideration of radial conduction[7] will reduce this to about 500°C, a temperature still excessive for practical application. Examination of Eq. (20-9) shows that δ is the only variable since $q'' = \text{const.}\ \phi(\delta)$. For the case of uniform heat sources, δ enters linearly into q''; therefore an increase of δ by a factor of 2 increases the heat flux by a factor of 2 and the temperature difference by a factor of 4.

The high energy deposition rates and resulting large instantaneous temperature rises as given in Table 20-2 dictated the selection of low-Z materials for beam absorption devices. Similarly, high heat fluxes force the adoption of small wall thicknesses and result in a special mode of heat transfer. For heat transfer surfaces at room temperature or slightly above, heat fluxes up to approximately 0.25 W/cm^2 can be handled by natural convection in air and thermal radiation. The Stefan-Boltzmann law for heat transfer by radiation between two surfaces separated by a vacuum is given as

$$q'' = \sigma(C_2 T_2^4 - C_1 T_1^4) \tag{20-10}$$

where $\sigma = 5.77 \times 10^{-12}$ W/(cm^2 °K^4) is the Stefan-Boltzmann constant, and C_1 and C_2 are constants depending on the orientation, distance, absorption, and reflection properties of the two surfaces.

For heat fluxes $0.25 < q'' < 10$ W/cm^2 forced convection with air yields good results and is usually inexpensive. Extensive heat transfer data for various surface geometries cooled by air jets are available.[8] As the heat flux is further increased, forced convection using water will yield satisfactory results. Heat fluxes of 50 W/cm^2 can readily be handled with moderate water velocities.

At water velocities of about 1.5 m/sec and heat fluxes of more than about 65 W/cm^2, another heat transfer mechanism becomes important. It is commonly referred to as boiling heat transfer. Extensive literature is available,[9,10] and only basic mechanisms will be reviewed here.

Air or water vapor bubbles trapped in crevices of the metal surface begin to grow in size as the metal surface temperature and, therefore, the temperature of the thermal boundary layer is increased to a point where bubble growth can be sustained. Depending on the velocity and temperature of the coolant, the bubbles will grow to a size such that they are swept away by viscous drag from the fluid, or they detach themselves due to their buoyancy. Some of the water vapor stays in the cavity and is the nucleus for the next bubble. Once in the main stream the bubbles will collapse more or less rapidly, depending on the subcooling, i.e., the temperature difference between the boiling point and the bulk fluid temperature. In highly subcooled liquids the bubbles can collapse without ever leaving the surface. This has important implications as will be shown later.

The vapor bubbles carry large amounts of energy away from the surface, through the thermal boundary layer and out into the main bulk fluid. Rather high heat fluxes can be handled in this fashion. Moreover, the moving bubbles stir up the thermal boundary layer and fresh bulk fluid reaches the hot surface. This mechanism is referred to as "nucleate boiling" and occurs in all energy absorbers discussed below.

As the heat flux is still further increased, the number of bubbles and the number of nucleation sites increase until adjacent bubbles start to interfere with each other's growth and motion. This is the condition of maximum heat flux, also referred to as critical or burnout heat flux. Any further increase of the surface temperature will result in the formation of a stable vapor film which, in turn, prevents the bulk liquid from reaching the surface and, thus, acts as an insulator. This condition is called "film boiling." It usually results in a rapid rise of the metal surface temperature to the point of destruction.

Unfortunately, the large number of variables, such as surface geometry and condition, fluid velocity and temperature, fluid properties, and radically varying heat transfer mechanisms for different regimes, make a single heat transfer correlation and prediction of burnout a very difficult task. No universally acceptable correlation yet exists. Furthermore, most experimental data reported in the literature are for the case of uniformly heated large surface areas. They do not adequately represent the local heat transfer conditions expected from impingement of high-intensity particle beams into solids. Typical values of burnout heat fluxes for moderate water velocities are in the neighborhood of 1 kW/cm^2.

High local heat fluxes from electron-bombarded water-cooled targets have been reported.[11] The values are much higher than the usual burnout heat fluxes. Boiling heat transfer experiments were also performed at SLAC[12] to establish permissible heat flux values from a local hot spot for different materials. Flat plates of varying thickness were bombarded with 15-keV

electrons from a tungsten filament. Heat fluxes of up to 6 kW/cm^2 were achieved, and the experiments confirmed that at least 2 kW/cm^2 could be assumed for the design and safe operation of energy absorbers, using either copper or aluminum. The experiments demonstrated clearly that the flow velocity parameter is only of secondary importance. It becomes significant only at the lower and upper boiling region limits. For example, an increase in flow velocity increases the burnout heat flux slightly. The subcooling of the fluid is a much more important variable and primarily determines burnout.

At this point an additional deleterious effect of operation at high heat fluxes will be mentioned. As already indicated above, highly subcooled boiling results in the collapse of the vapor bubble either on or very close to the material interface. The collapse or cavitation of a bubble will give rise to a shock wave that expands radially and dissipates its energy as it propagates. If the bubble cavitates very close to the surface, the shock wave is strong enough to work-harden the metal. The surface will become brittle and will eventually fail from fatigue. Cavitation or dynamical erosion can be very severe; it is often accelerated by thermochemical and other corrosion mechanisms. Observed erosion rates per 100 hours and for heat fluxes of 1.5 to 2.0 kW/cm^2 were 0.02 cm for a 1100 series aluminum plate, 0.0012 cm for a 6061-T6 series aluminum plate, and 0.0065 cm for a tungsten plate. Comparable damage was observed for various pure copper plates. Solutions to the erosion problem are proposed in a later section.

Thermal stress development

It has been demonstrated that high rates of energy deposition can be achieved with the accelerator and that the instantaneous energy dissipation during a single pulse gives rise locally to steep temperature gradients in space and time.

If the body under consideration and its properties are continuous, the nonuniform temperature distribution will give rise to thermal stress and strain within it. Each volume element of the body tends to expand (or contract) by a different amount proportional to its temperature rise (or temperature drop). Since the temperature change is nonuniform, adjacent volume elements will change by different amounts. In a continuous body, adjacent volume elements will hold the element under consideration in place and shape, i.e., they represent an internal constraint. The result is what is called "thermal stress." External constraints, i.e., body forces, can also cause thermal stress in a heated body. The designer is warned not to ignore them; they can fundamentally influence the performance of a specific structure! The expansion resulting from the temperature rise is called "strain," denoted by ε. It is the same in all directions in an isotropic body and is related to the temperature change, ΔT, and to the coefficient of linear thermal expansion, α, by the relationship

$$\varepsilon = \alpha \, \Delta T \tag{20-11}$$

The stress, σ, is related to the strain by Hooke's law, assuming a fully elastic system:

$$\sigma = E\varepsilon = E\alpha\,\Delta T \tag{20-12}$$

where E is the modulus of elasticity.

If in addition, external forces are applied, the resulting stresses are superimposed on the thermal stresses. Hooke's law can then be expressed as[13]

$$E\varepsilon_{xx} = \sigma_{xx} - \nu(\sigma_{yy} + \sigma_{zz}) \tag{20-13a}$$

$$E\varepsilon_{yy} = \sigma_{yy} - \nu(\sigma_{zz} + \sigma_{xx}) \tag{20-13b}$$

$$E\varepsilon_{zz} = \sigma_{zz} - \nu(\sigma_{xx} + \sigma_{yy}) \tag{20-13c}$$

$$\varepsilon_{xy} = \frac{1}{2G}\sigma_{xy} \qquad \varepsilon_{yz} = \frac{1}{2G}\sigma_{yz} \qquad \varepsilon_{zx} = \frac{1}{2G}\sigma_{zx} \tag{20-13d}$$

and

$$G = \frac{E}{2(1+\nu)} \tag{20-14}$$

where ν is Poisson's ratio and G denotes the shear modulus. Addition of Eq. (20-12) to Eqs. (20-13a) through (20-13c) yields the total stress.

Thermal stresses are usually compressive (negative) stresses in the center of the heated area, and tensile stresses outside the heated area. For steady-state conditions the designer can allow for combined stresses up to the yield limit of the particular material. In the design of structures the ductility is often allowed to relieve stresses, using typical 0.1 to 1.0% permanent deformation values as design criteria. This may be disastrous in thermal stress applications and does not present a solution to the problem. It should be pointed out, however, that the detrimental effects of thermal stresses are more often than not overestimated. Moreover, stress values can be lower or higher than predicted by Eq. (20-12), depending on geometry or sources of stress concentration. A wide variety of thermal stress problems has been treated analytically.[14]

Thermal fatigue

The pulsing electron beam will result not only in a nonuniform, spatial, temperature distribution but will also cause temperature variations in time. Thus, cyclic stresses of thermal origin are superimposed on the steady-state thermal stress distribution, and thermal fatigue may result. Under these circumstances, structures fail at much lower stresses than predicted by simple stress–strain relationships. Ductile materials relieve stresses in excess of the yield strength by plastic deformation and creep. Thermal fatigue damage then is caused by cyclical yielding or cyclical plastic deformation.

The first signs of onset of thermal fatigue are an elongation of certain crystals and a slip at the grain boundaries. Under continued cyclical load, the slip eventually develops into individual pores, and cracks appear. If additional external constraints exist, fracture of the structure may result. The magnitude of the stress necessary to cause failure in the structure diminishes with increasing number of cycles. The fatigue or endurance limit of the material is determined by the number of cycles required to generate cracks at the given elevated temperature, as described above.

Electron accelerators can typically produce 10^{10} pulses/yr, and long-term fatigue values have to be selected accordingly.

Superposition of cycling and steady-state stresses and prediction of the expected lifetime can be accomplished using, for example, a Goodman diagram, described in more detail in another section below.

Thermal shock

A number of accelerators exist that can produce bursts of very high-power density over short periods of time. The high rates of energy dissipation during the pulse give rise to very steep temperature gradients in space and time, resulting in proportional thermal stress gradients. The latter can cause formation of thermal shock waves which, in turn, may result in fracture and spallation of materials, regardless of how well the part is cooled.

An experiment to determine the importance of this effect on an aluminum collimator module is described in more detail below. The rate of energy deposition during the pulse in the module wall was 600,000 kW/cm^3. No damage was observed. This may be explained by the relatively high ductility of the aluminum; another, more brittle material may have failed.

20-2 High-power beam dumps (DRW)

This section discusses the important design criteria and features of the high-power A-beam dump D-11 (see Fig. 17-1) and beam dump east D-400. Emphasis is given to the three important dump components: the window, the "vortex flow" region, and the plate compartment. The auxiliary but important problems of radiolysis in water, the evolution of free hydrogen and its disposal, are also treated in detail.

Criteria

The high-power beam dumps are to be capable of continuously absorbing and dissipating the full beam power produced by the SLAC linac over a wide range of energies. This includes conditions arising from radiators placed in the beam transport system upstream of a dump. Table 20-3 gives a summary of the most important criteria.

Table 20-3 High-power beam dump criteria

1. Full average beam power	2.2 MW
2. Incident beam energy	$\leq$25 GeV
3. Minimum beam size	
For A-beam dump	$\sigma_{b,x} = 0.1$ cm; $\sigma_{b,y} = 0.25$ cm
For beam dump east	$\sigma_b = 0.25$ cm
4. Entrance window size	15-cm diameter usable area
Thickness	0.127 cm
5. Total length	30 radiation lengths
6. Dump diameter	140 cm
7. Dump shell material	Stainless steel Type 316-L
8. Distance of beam center line from radial boundary	34.5 cm minimum
9. Water pressure at the window	45 psia maximum
10. Cooling water flow velocity in vortex region normal to beam direction	100 cm/sec ($\approx$3 ft/sec) minimum
11. Minimum flow rate	
For high-power operation	2000 liters/min (=550 gal/min)
For low-power operation	1500 liters/min (=400 gal/min)
12. Maximum cooling-water temperature	40°C
13. Window is remotely replaceable	
14. Water drainage is possible in place	
15. Gas is continuously vented from the dump vessel into the closed, radioactive, water loop	

Important design features

An isometric view of a high-power beam dump is shown in Fig. 20-3. One can identify four major components: (1) the beam entrance window; (2) the 10-radiation-length "vortex" flow region; (3) the 20-radiation-length plate compartment; and (4) the support carriage. The window is treated in detail in a separate section below.

It has been demonstrated in a previous section that only low-Z materials can be used to degrade and dissipate a 2.2-MW beam. In order to retain flexibility for beam power or energy variations and to achieve operational safety at a reasonable construction cost, it was decided to dissipate most of the beam power and establish the shower maximum in a large volume of water.

The beam enters into the cylindrical vessel through a thin window which is located off-axis, at $R = 30$ cm. The beam then traverses the vessel parallel to the axis of rotational symmetry. The shower maximum for 20-GeV electrons occurs at a depth of approximately 170 cm. For stagnant water conditions, the temperature would rise rather rapidly. Therefore, good circulation and mixing are required to prevent local overheating near the origin of the beam, particularly at the shower maximum where volume boiling could

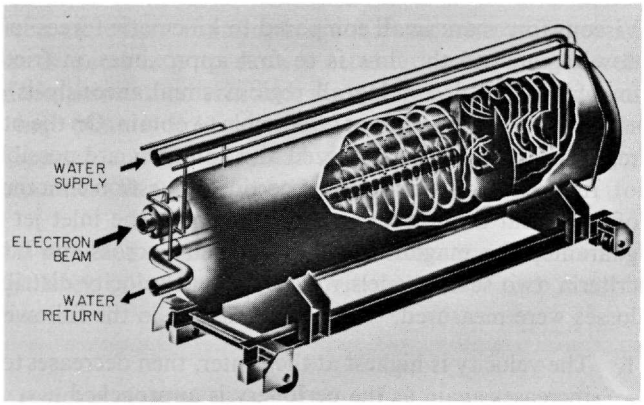

Figure 20-3 Artist's conception of a 2.2-MW ($E_0 = 11$–25 GeV) beam dump.

occur. Formation of a gas space would reduce the effective Z drastically; it would shift the shower maximum downstream and could result in destruction of the plate compartment in the rear of the dump. Hydrogen formed in the radiolysis of water could come out of solution and might present additional complications. Thus, the exposure of a volume element of water to the hot core of the beam has to be limited to a few pulses at most.

Several methods could be applied to exchange the water continuously in the cylinder. In order to economize on the flow rate and to reduce the beam exposure time of a volume element of water, it was decided to use a "vortex" flow. An inlet flow header located at the periphery of the shell induces the vortex flow. Water is injected through a series of holes, equally spaced over the 10 radiation lengths. The water then flows spirally toward the center of the vessel where the exit manifold is located. The velocity normal to the nominal beam center line (at $R = 30$ cm) was set at approximately 100 cm/sec. For this velocity no volume element of water equal in size to the hot core of the beam is exposed to more than about 4 pulses.

Knowledge of the quantitative radial velocity distribution is essential to guarantee safe operation. Seven different flow regions have been identified and are listed as follows:

1. The boundary layer at the cylinder wall
2. The rotational flow as a result of the submerged nozzle
3. The potential vortex flow region (perturbed by the effect of the geometric disturbance due to the inlet nozzle)
4. The interface between regions 2 and 3
5. Regions 4, 2, and 1 for the outlet nozzle in the center.

Losses in the system are mainly frictional losses in the various boundary layer regions due to shearing forces and eddy mixing losses from jets and wakes.

Viscous forces are small compared to kinematic forces in the potential vortex flow region and the flow is to first approximation frictionless. The mathematical model describing all regions simultaneously is complicated and its solution very difficult if not impossible to obtain. On the other hand, individual regions can readily be analyzed and solutions are possible.

In order to answer the most pertinent question concerning the performance of an actual beam dump, namely, what is the inlet jet velocity required to guarantee the magnitude of the velocity across the beam set forth in the criteria, two scale models were built and velocity distributions and pressure losses were measured.[15] The tests resulted in the following conclusions:

1. The velocity is highest at the center, then decreases to a flat minimum and increases again as the periphery is approached.
2. The ratio of the velocity at the beam to the inlet jet velocity is, to first approximation, independent of the Reynolds number over a wide range of N_{Re} (only the velocity was varied, however).
3. The velocity ratio varies linearly with the ratio of nozzle diameter to nozzle spacing.
4. A central outlet nozzle has a stabilizing influence on the flow and its symmetry.

Conclusion 1 indicates that the flow pattern is not just a simple potential vortex, given by $V \cdot r = \text{constant}$, but contains a term for solid angular rotation. This was to be expected due to the presence of other flow regions as described above. On the other hand, angular momentum is conserved to a large degree.

Conclusion 4 deserves some further comments: for the potential vortex under consideration the sink is located at the center of the vessel. In principle, no outlet nozzle has to be present along the center. Omission of the outlet pipe and creation of an outlet nozzle at the end of the vessel would change the two-dimensional vortex into a three-dimensional one. This is analytically predictable and was experimentally verified. In the case of a stable flow pattern the results indicated little difference in the velocity at the beam location between presence and absence of the outlet nozzle. Presence of the pipe, however, stabilized the flow appreciably and reduced asymmetry due to the perturbation caused by the geometric disturbance of the inlet nozzle. The axis of the inlet manifold coincides with a horizontal plane through the rotational symmetry axis of the vessel. This location gave best results at the beam axis. The diameter of the dump cylinder was determined by radial shower development considerations.

The 20-radiation-length plate compartment will now be described. Since space is at a premium and large pieces of equipment are expensive to fabricate and difficult to handle, it is not economical to attenuate fully the cascade shower in water alone. Solid copper plates are introduced downstream of the shower maximum, at a location where the cascade shower is sufficiently attenuated to cause only moderate heat fluxes and temperature rises.

A total of nineteen plates are contained in the compartment. They are graduated in thickness according to shower attenuation to maintain the design heat flux and temperature criteria and, thus, optimize the total length of the vessel. The first plate is 0.32 cm thick, the last one 3.8 cm. The plates are equally spaced and water-cooled at about 200 cm/sec water velocity. The maximum heat flux anywhere in the system is 2 kW/cm^2 (for $P_{AV} = 2.2$ MW).

The dump vessel is mounted on a mobile frame to allow remote placement or removal, since high levels of induced radioactivity will in due time result in inaccessibility of the area.

Window and window removal system

It has already been mentioned that the beam enters the dump through a thin window. The use of a window is necessary because the stainless steel vessel shell, which is approximately 1 cm thick, is not capable of dissipating all the power deposited in it. The size of the window is determined (a) by the maximum possible beam deviations from the nominal center line, (b) by the aperture of a protection collimator upstream of the dump, and (c) by the momentum spread of the residual electron beam due to a 0.01-radiation length target. The effective window area normal to the beam is defined by a 15-cm diameter circle.

High-purity copper (with thin layers of nickel and hard chromium plating as discussed below) was selected as window material. It is compatible with the rest of the system, which contains only copper and stainless steel. Based on peak power deposition, aluminum or titanium would have been superior to copper (see Tables 20-1 and 20-2). However, in an aqueous system aluminum would not be compatible with the copper used in the plate compartment, and titanium presents more fabrication problems than copper. The disadvantage of copper due to its high Z is offset, in part, by its excellent thermal conductivity.

The window thickness was chosen to be 0.127 cm (0.050 in.). The window separates water at elevated pressure from the beam transport vacuum system. To minimize the stress level, a hemispherical shape was adopted. The power deposited in the window can be readily calculated from a modified form of Eq. (20-6):

$$P = 1.6 \times 10^{-19} N \delta \rho \frac{dE}{dx} \tag{20-15a}$$

or

$$P = I_{AV} \delta \rho \frac{dE}{dx} \tag{20-15b}$$

where N is the number of electrons per second, δ is the window thickness, ρ the specific gravity, and I_{AV} is the average beam current.

For $E_0 = 11$ GeV and $P_{AV} = 2.2$ MW, the total power deposited in the window is $P_w = 0.325$ kW. The minimum expected beam size at the A-beam dump (D-11) is approximately 0.1 cm^2. The resulting heat flux into the water is about 2 kW/cm^2 (this includes consideration of lateral conduction in the window). Assuming steady state and the proper boundary conditions, solution of Eq. (20-8) yields a maximum temperature difference across the window of about 32°C. The thermal stresses are moderate (for a water-cooled window, taking into account the temperature difference across the interface) but would be severe if such a small beam cross section existed continuously at full power operation. A separate window-cooling mechanism was developed. Individual jets of water impinge in the area of high heat flux and prevent development of burnout conditions.

The window is expected to be the weakest item in the beam dumps. The production costs of a dump are high and lead times are long. For these reasons, it was decided to make the window exchangeable. Two seals are required: one between water and air, and the other one between vacuum and air. In the high radiation environment, only all-metal joints are useful for extended service. After extensive evaluation of various all-metal joints, the knife-edge-type of vacuum joint was chosen for both the vacuum and the water side of the window. It employs copper for the window, which also serves as the gasket, and stainless steel for the knife-edge flange. These are the same materials as are used in the rest of the dump. The knife-edge gasket has the advantage that it will seal vacuum tight, even with shallow scratches on the knife-edge or the gasket. Thus, neither the knife-edge nor the gasket is critical for a successful seal.

The expected high levels of induced radioactivity will result in inaccessibility of the dump, and, consequently, the window must be remotely exchangeable. For this purpose a hydraulic–pneumatic remote window-removal mechanism was developed and successfully tested. In order to reduce the complexity of this mechanism, only two bolts are used to tighten the flanges and make the seal. The flanges are, therefore, very stiff to achieve successful sealing. The bolts are turned by means of a hydraulically manipulated, pneumatic impact wrench, and windows are exchanged by employing a hydraulically operated mechanism. Detailed instructions for removal of the window unit have been prepared.[16]

A full-size prototype of a window was tested in the National Bureau of Standard's linac.[17] Temperatures were measured with thermocouples attached to the air side of the window. The highest heat transfer rate from the window to the water was approximately 1.25 kW/cm^2 in the area of beam impingement. The highest temperature recorded was 315°C. This thermocouple did not, however, coincide with the beam center line, and temperatures may have been as high as 350°C. Furthermore, the data are not corrected for beam exposure of the thermocouples. This would lower the values. The window showed no spallation effects due to thermal shock, and the hard-chromium plating on the water side appeared to be undamaged.

Material selection and fabrication

The dump vessels, including all the piping, are fabricated from stainless steel, Type 316-L. This material was selected because of its superior corrosion resistance. It is a fully austenitic, low-carbon steel which is Mo-stabilized. Carbide precipitation in the multitude of welds is negligible and corrosion resistance in these areas is very good. Furthermore, Type 316-L appears to be less susceptible than type 304 to stress corrosion cracking, frequently the swift destroyer of stainless steel structures.

All welds were made by the tungsten inert gas arc method (TIG) to highest welding quality standards. Only low-carbon, Type 316-L welding rod was used. Full penetration and fusion were required, since the lack of either may cause crevice corrosion, subsequent stress-corrosion cracking, and pit corrosion. All welds were inspected using x rays and dye penetrants.

The plates located in the rear of the vessel are oxygen-free high-conductivity copper, graduated in thickness as previously described. Without surface treatment the cavitation erosion problem would be a serious limitation on the expected lifetime of a beam dump. Experiments have indicated that hard materials are much less subject to cavitation erosion than soft ones. Good results were achieved by electroplating the copper surface with a sandwich of nickel and hard chromium. The soft nickel layer is approximately 0.0025 cm thick, the hard chromium layer about 0.001 cm. There are two reasons for the nickel substrata. First, it seals the copper surface and protects it from various corrosion mechanisms; this is important, since hard chromium is susceptible to cracking. Second, the soft nickel layer acts as a stress-absorption buffer. Significant differences in the coefficient of linear thermal expansion between copper and chromium would cause large thermal stress concentrations at the interface during operation. The chromium would crack and might even flake off. The nickel layer, in turn, is soft, can yield easily, and has a thermal expansion coefficient which is intermediate to the coefficients of copper and chromium. It is of importance to mention that the hard chromium has to be plated above 55°C, otherwise continuous microcracks are formed and the plating is porous.

The beam dump prior to installation is shown in Fig. 20-4. The right-hand side of this front view shows the water inlet manifold at the top, then the water outlet manifold, and a drainage line at the bottom. Also shown as part of the water outlet manifold is a Venturi for removal of air during the filling procedure and for continuous venting of gases formed in the radiolytic decomposition of water.

The water system and corrosion problems

The radioactive cooling-water loops are described in detail elsewhere in this text, and a brief treatment will suffice here. The water quality of the primary radioactive water loop is monitored daily. A resin ion-exchanger located in

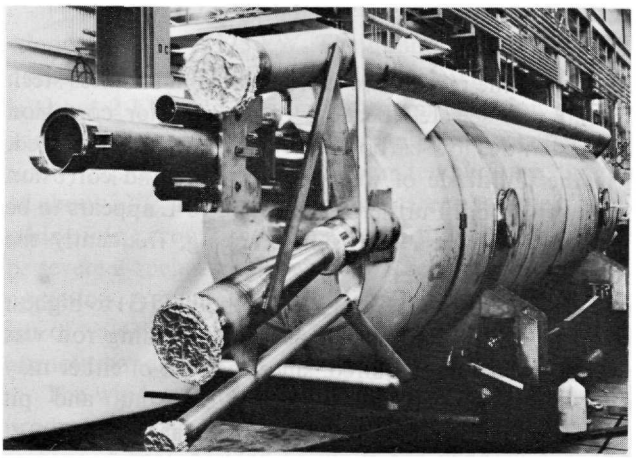

Figure 20-4 Front view of 2.2-MW beam dump (D-400).

a bypass loop serves to keep the water at 1 megohm-cm, or better. The pH is kept slightly acidic, approximately 6.2–6.5, from carbon dioxide dissolved in the aerated water. Particular attention is given to chlorides in the water, since they are a major factor in initiating stress-corrosion cracking in stainless steels. Chloride concentrations are <1 ppm. Based on extensive experimental results from other laboratories, it is felt that chloride concentrations should not exceed 0.1 ppm for safe, long-term operation. Significant amounts of hydrogen peroxide, H_2O_2, are formed in the radiolysis of water. It is an oxidizing agent and, therefore, caused concern about the corrosion resistance of the materials used in the radioactive loops. A study of H_2O_2 chemistry indicated that no problems should exist in the water loops. Stainless steels as well as aluminum alloys derive their superior corrosion resistance from the presence of a dense, more-or-less insoluble, oxide film on the surfaces of these materials. Aluminum containers are often used to store H_2O_2 and keep it from decomposing. It is felt that the presence of H_2O_2 in the radioactive water loops either enhances formation of even denser oxide films or has no influence at all on the corrosion behavior of these systems.

A major concern during maintenance work has been the radiation from curies of ^{7}Be (54 days half-life), a daughter nuclide of ^{16}O. It is formed in not negligible quantities in the beam dumps under high-power operation. Measurements revealed that essentially all ^{7}Be is trapped in the ion exchangers, thus localizing the radiation problem and making it easy to shield against.

The tritium (^{3}H) buildup in the radioactive water systems is also monitored. The total volume of water contained in the A-beam dump radioactive waterloop is approximately 12,000 liters. It was estimated that about 5 MW-hr were dissipated in this volume during the first 9 months of operation. At the end of this period the ^{3}H level was 3×10^{-4} $\mu Ci/cm^3$ or about 4 mCi for

the total system. The maximum permissible concentration (MPC) for disposal of water into sewers is 10^{-3} μCi/cm^3. Thus, drainage of the water at regular intervals is an inexpensive solution to minimize health hazards.

Operational experience

To date (July 1967), after 12 months of continuous operation, no failures have occurred. The highest average power deposited and dissipated in the A-beam dump so far is 240 kW at 17.5 GeV (on March 28, 1967).

Radiolysis and radioactivity in the water

Large quantities of water are used in the beam dumps as the coolant and primary energy absorbant. In the high-power beam dumps, approximately 90% of all the energy entering the dumps is dissipated directly in the water, with the remaining 10% dissipated in the copper plates, and a very small part lost from the system due to radiation. For electrons with energies $E_0 > 0.5$ MeV, the linear energy transfer, i.e., the amount of energy lost per unit distance traveled is $-(dE/dx)\rho \approx 2$ MeV/cm. This energy is lost in discrete amounts averaging about 100 eV per event. The energy usually converts within less than 10^{-12} sec into heat. Water molecules are excited in the region where this energy transfer occurs; such a region is called a spur. The energy deposition reaches a maximum at the end of the track of a charged particle and results in formation of a high-temperature region, called a "thermal spike." For this case, spurs will be an average of 5×10^{-5} cm apart.[18]

During the pulse, high concentrations of free radicals such as H and OH are formed in the spur. Some of these radicals will react with one another; others diffuse out of the spur into the bulk water. The reactions within the spur will yield H_2, H_2O, H_2O_2, and others. They can be symbolically represented as

$$H_2O \rightarrow H, H_2, OH, HO_2, H_2O_2, H_2O, e_{aq}^- \qquad (20\text{-}16)$$

where e_{aq}^- is the hydrated electron.

The radicals diffusing into the bulk can increase in concentration to a point where they not only react with the H_2, H_2O, and H_2O_2, but also with one another to form more H_2 and H_2O_2. Since the solubility of hydrogen in water is only about 0.8×10^{-3} moles/liter, after a certain time there will be a net evolution of free hydrogen. Also, once equilibrium concentration is reached, hydrogen peroxide is expected to decompose due to radiation and other chemical reactions, and a net evolution of O_2 can be expected. Theoretical quantitative prediction of evolution rates is a complicated task. It is thought that at least fourteen rate equations have to be solved simultaneously.

Measurements have been made[19] to determine the amount of free hydrogen produced using an electron linac giving pulses of approximately 7×10^4 g-rads and energies $E_0 \approx 15$ MeV. The dose into the effective irradiated volume

of 15.3 ml of oxygen-free water was approximately 4.5×10^3 rads. A constant yield $G(H_2) = 0.71$ molecule of H_2 per 100 eV of energy absorbed was observed. These authors also calculated the direct yield from oxygen-free water. This yield $g(H_2)$, which does not include contributions from secondary reactions, was found to be 0.41. The calculated result for 0.8 N H_2SO_4 (N stands for normal concentration) was $g(H_2) = 0.45$. Using $G(H_2) = 0.70$, the calculation yields a total rate of H_2 evolution of 1.6 liters/(MW-sec) from the SLAC high-power dump. Whether or not this G value holds at much higher energies and current densities than discussed above has not been determined. However, it is thought[20] that the true value will lie within a factor of 2 of $G(H_2) = 0.70$, which would amount to a range of 0.8 to 3.2 liters H_2/(MW-sec). Impurities contained in any real operating water system have a marked effect on reaction rates and many influence $G(H_2)$ significantly.

Various degassed neutral and alkaline aqueous solutions have been irradiated[21] with γ rays from a ^{60}Co source and with 2-MeV x rays. The results were the same for the neutral and the alkaline solutions, and they were independent of temperature from 4° to 65°C. The direct yield was $g(H_2) = 0.45$. Degassed acidic solutions of light water (0.4 M H_2SO_4, where M denotes molar concentration) and heavy water (0.4 M D_2SO_4) were irradiated with γ rays from a ^{60}Co source,[22] and a direct yield of $g(H_2) = 0.45$ and 0.38 was measured for the light and heavy water samples, respectively.

The hydrogen yield from air-saturated water has been calculated[18] for the initial condition where H_2 and H_2O_2 concentrations are very small compared with O_2. The result is $G(H_2) = 0.16$. This means that if $g(H_2) = 0.45$ as reported above is correct, the difference between 0.45 and 0.16 is lost due to secondary reactions of H_2 with OH. Oxygen-saturated water has been irradiated with γ rays from a ^{60}Co source, and an initial yield of $G(H_2) = 0.20$ was measured.[23]

Experiments have been performed at SLAC[17] to measure the rate of H_2 evolution in the high-power A-beam dump. The beam dump radioactive water system is a closed-loop system with a surge tank, pump, and heat exchanger. Hydrogen produced by radiolysis evolves in the aerated gas space on top of the surge tank and its concentration is measured in a sampling loop. The H_2 evolution has been evaluated for incident electron energies of 10.0, 12.0, and 16.3 GeV; pulses of 6×10^6 to 5.4×10^7 g-rads; and average power deposited in the dump ranging from 20 to 170 kW. The rates of H_2 evolution varied from 0.26 to 0.44 liter/(MW-sec) with an average of 0.31 liter/(MW-sec). The latter corresponds to $G(H_2)_{AV} = 0.14$. It seems that at these high power densities, reactions occur which tend to favor recombination of free radicals to form H_2O. However, agreement with the values for aerated water reported above is quite good.

The free hydrogen evolving in the surge tanks presents significant problems. The lower explosive limit of a hydrogen–air mixture is 4% H_2 for atmospheric conditions (STP). One can consider 2% H_2 as the upper limit for safe, continuous operation. For water already saturated with H_2 it took

only 10 min to reach the safe limit at $P_{AV} = 150$ kW. Unfortunately, even at low average power levels of, for example, 50 kW the amount of radioactivity released into the atmosphere is prohibitive for any long-term venting operation.

The SLAC Health Physics Group has analyzed the gases on top of the surge tank during several experiments and identified ^{15}O (2 min) and ^{11}C (20.5 min) as major contributing isotopes; both are daughter nuclides of ^{16}O. A drying column failed to remove the ^{15}O, suggesting that it is in gaseous form (O_2) rather than in the H_2O molecules of the water vapor. Chemical removal of CO and CO_2 indicated that virtually all ^{11}C is in CO_2. The radiation level at a distance of 100 cm from the top of the surge tank was ≈ 60 R/hour for steady-state dissipation of 170 kW in the dump.

Two solutions have been proposed for removal of evolved hydrogen: a chemical CO_2 removal-storage-venting system and a catalytic recombination system. In the first system gases coming off the surge tanks are diluted to achieve concentrations of $<2\%$ H_2. Then ^{11}C is removed by absorbing CO_2 in a resin bed. Thereafter, the gases pass through a storage tank large enough to guarantee a lapse time of 12 to 15 half-life periods for ^{15}O before they are finally vented into the atmosphere. After careful study, this system was rejected in favor of a catalytic recombination system. It consists of a fully closed system in which the gases are diluted to maintain concentrations of less than 2% H_2. The gases are continuously recirculated through a catalytic bed, in which H_2 and O_2 are recombined to form water. A SLAC-developed recombiner prototype is successfully operating at this time (July 1967). High recombination efficiencies have been obtained at slightly elevated temperatures.

20-3 Low-power beam dumps (DRW)

Two types of low-power beam dumps are discussed in this section: (1) the tune-up beam dump (D-10) and the central beam dump (D-2); and (2) the B-beam dump.

The tune-up dump is located in the space between the central beam and A-beam as indicated in Fig. 17-1. Its horizontal dimensions were chosen so as to allow maximum possible momentum acceptance during accelerator tuning. Crude spectrum measurements are possible by means of a spectrum monitor (S-10) located in front of the tune-up dump. The monitor consists of a row of secondary-emission monitor (SEM) foils and is described in more detail in Chapter 19. The power absorption capacity of the dump was determined by two machine requirements. First, the dump should accept a beam at the full repetition rate (360 pulses/sec) and with a peak current of ≥ 1 mA to satisfy the minimum requirements for proper functioning of the accelerator phasing system and the beam position monitors. Second, it should also accept a tune-up beam at full energy and full current (50 mA for Stage I). For a dump of reasonable size and cost, this requires a reduction in the beam

repetition rate to approximately 10 pulses/sec. With the inclusion of a safety factor, the maximum average power absorption capacity was set at 60 kW.

Although the power absorption specifications for the central beam are somewhat lower than for the tune-up beam, it was decided to duplicate the tune-up beam dump for this application and thus reduce engineering costs.

The B-beam dump is located in the B target room and serves to absorb and dissipate the electron beam and as the μ-meson target. Its power absorption capacity is 120 kW.

Table 20-4 shows a summary of the important criteria of the low-power beam dumps.

Design features, materials, and fabrication

In the tune-up and central beam dumps, beam power is dissipated in a series of water-cooled, high-conductivity copper plates. They are graduated in thickness according to shower development and attenuation, thus optimizing

Table 20-4 Low-power beam dump criteria

Characteristics	*Tune-up and central beam dumps*	*B-beam dump*
Maximum average beam power	60 kW	120 kW
Incident beam energy	$\leq$25 GeV	$\leq$20 GeV
Minimum beam size	$\sigma_b = 0.3$ cm	$\sigma_b = 0.3$ cm
Entrance window size	15 × 48 cm	15 × 30 cm
Thickness	0.16 cm	0.32 cm
Total length	30 radiation lengths	20 radiation lengths
Dump diameter	—	35.5 cm
Width	49.5 cm	—
Height	16.8 cm	—
Dump shell material	Stainless steel Type 316-L	Stainless steel Type 304-L
Window material	Stainless steel Type 316-L	OFHC[a] copper
Plate material	OFHC[a] copper	OFHC[a] copper
Nominal distance of beam center line		
From horizontal boundary	$\geq$1.9 cm	—
From vertical boundary	7.3 cm	—
Water pressure	165 psi	—
Cooling-water velocity between plates	230 cm/sec ($\approx$7.5 ft/sec)	150 cm/sec ($\approx$5 ft/sec)
Minimum flow rate	130 liter/min ($\approx$35 gal/min)	150 liter/min ($\approx$40 gal/min)
Maximum inlet cooling-water temperature	25°C	

[a] Registered trade name of American Metals Climax, Inc.

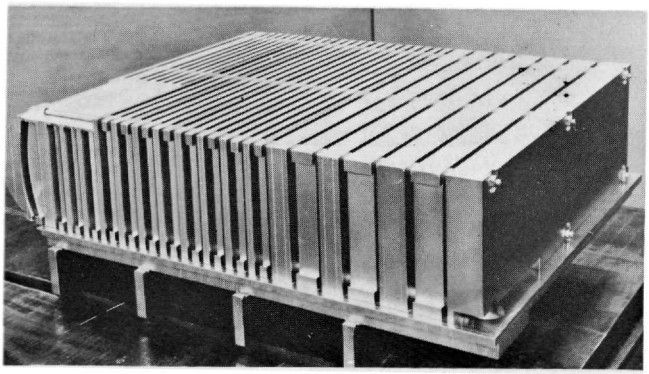

Figure 20-5 Plate compartment of 60-kW tune-up beam dump (D-10).

the dump length. Figure 20-5 shows a partial assembly of a tune-up dump. All plates are covered with electrodeposited layers of nickel and hard chromium for cavitation–erosion protection as described in detail in the previous section. The plates are contained in a Type 316L stainless steel shell.

The lateral dump dimensions were selected to allow a reasonable margin for possible beam excursions, taking into account radial power escape and heat transfer and thermal stress in the stainless steel sidewalls.

The window is a portion of a cylindrical surface to minimize the wall thickness and, consequently, the power absorption. For fabrication reasons, stainless steel has been selected in preference to copper as the window material. The window has been arc welded (TIG) to the stainless steel sidewalls. Copper would have required a more expensive brazing operation. The smaller wall thickness combined with the capacity for operating at much higher thermal stresses partially offsets the disadvantage of stainless steel because of its low thermal conductivity compared to that of copper. Figure 20-6 shows the completed tune-up dump assembly mounted under its support flange and ready for installation in the divergent vacuum chamber.

The B-beam dump is circular in cross section. It has a flat plate copper window, furnace-brazed to a stainless steel flange. The latter is welded to the stainless steel plate compartment. Other features are very similar to the tune-up dump design and are, therefore, not described further.

Operations to date

Experience during the first year of operation of the beam dumps has been flawless. The maximum average powers deposited in the tune-up beam dump and the central beam dump were about 40 and 45 kW, respectively. The B-beam dump has dissipated up to 75 kW.

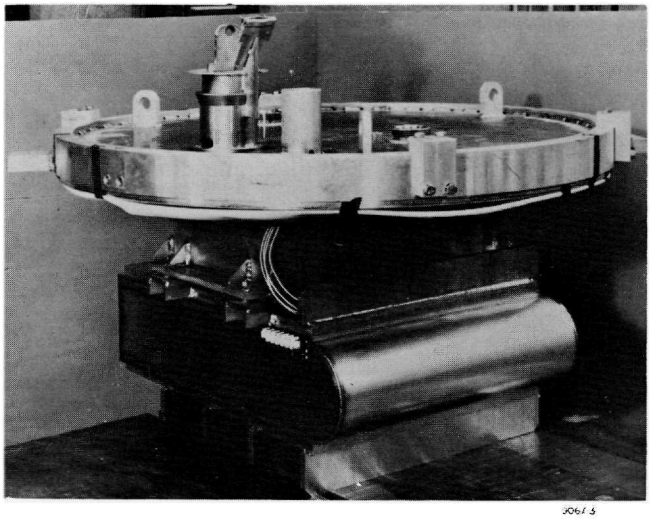

Figure 20-6 Assembly of 60-kW tune-up beam dump (D-10).

20-4 Collimators and slits (DRW)

General considerations and definitions

A list of important components in any beam transport system almost always includes collimators and slits. The functions of these devices may be described as follows: collimators are used to define the spatial extent of the particle beam, to form aperture stops for beam transport systems, and to protect magnets and other equipment from physical damage by the beam; slits are similarly used to provide stops that define momentum transmission in a beam transport system containing dispersive elements.

In the following sections three basically different types of collimators and slits will be treated in detail: (1) the variable-aperture, high-power collimator and slit; (2) the variable-aperture high-Z collimators and slits; and (3) the fixed-aperture protection collimators. Either variable or fixed-aperture collimators are employed depending on their function in the beam transport system. For example, at the beginning of the beam switchyard and the beam transport system, a set of variable-aperture collimators define the beam cross section at the center of the pulsed magnets PM-1 through PM-5. (For locations see Fig. 17-1.)

Under normal operation the power absorption in the collimators should be relatively low compared to the total beam power. However, mis-steering of the beam, beam breakup at the end of the accelerator, or misalignment of the collimators can cause abnormally high-power densities to be absorbed by these devices, which must, therefore, be designed to operate in this condition for an extended period of time without suffering physical damage.

Most components in the beam transport system must be protected from excessive power deposition or excessive exposure to primary radiation. Their location and aperture are usually fixed and, consequently, they may be protected by fixed-aperture collimators installed in front of them.

The slits are of variable aperture to satisfy the varying demands on maximum allowable momentum spread of the beam for different high-energy physics experiments. A relatively high-power absorption may occur when a narrow momentum spectrum of the electrons is desired and significant momentum components must be removed, or when the output of the accelerator is unstable.

Since one of the prime objectives of slits and collimators is the removal of particles of unwanted momenta from beam transport systems, it is of utmost importance to select a proper geometry and/or suitable materials. A poor choice of the latter may result in excessive multiplicity along the beam-defining edges and in the introduction of a new, significant momentum spread into the beam. This could reduce or even nullify the benefits of momentum selection in the beam transport system.

It would seem that optimum results can be achieved by using a high-Z material and a short physical length. This statement contains some element of speculation and more experimental work is needed to determine the effect of physical length on slit scattering. In the paragraph on shower development in Section 20-1, it has been demonstrated that high-Z materials are not useful for continuous dissipation of a full-power SLAC beam. Therefore a compromise has to be made on Z which results in an increase in physical length of the slits.

Ideally, the length of a slit should be zero, i.e., the slit should coincide with the image of the center of the pulse magnet group (PM-1–5) formed by the quadrupole doublet (Q-10, Q-11 or Q-30, Q-31). The size of this image and consequently the resolution at the slit is a function of the particle beam size at the center of the pulse magnet group. After passing through the quadrupoles (Q-10 and Q-11), the beam is bent a total of 12° by the first bending magnet group in the A-beam transport system (B10 through B13), and the beam is thus dispersed for momentum analysis at the slit. The dispersions at the A-beam slit (SL-10) and at the B-beam slit (SL-30) are 0.177%/cm and 0.343%/cm, respectively. Only a horizontal slit is needed to remove dispersive components of the beam, since the beam spectrum is displayed as a function of momentum in the horizontal plane.

20-5 High-power collimator and slits (DRW)

In the following section the high-power collimator (C-1) and slit (SL-10) are discussed. For locations see Fig. 17-1. An analysis of a slit is presented applying the principles and equations given in Section 20-1. Corrosion problems arising in a stainless steel–aluminum–water system are treated in

Table 20-5 High-power collimator and slit criteria

Maximum average beam power	
For minimum beam size	1.0 MW
For average expected beam size	2.2 MW
Incident beam energy	$\leq$25 GeV
Minimum beam size (for $\Delta p/p = \pm\frac{1}{4}\%$; angular divergence $\Delta\theta = 10^{-5}$ radian)	
At collimator C-1	$\sigma_b \geq 0.1$ cm
At slit[a] SL-10	$\sigma_{b,x} = 1.58$ cm; $\sigma_{b,y} = 0.08$ cm
At slit SL-30	$\sigma_{b,x} = 0.79$ cm; $\sigma_{b,y} = 0.07$ cm
Average expected beam size	
At the collimator	$\sigma_b \approx 0.3$ cm
At slit SL-10	$\sigma_{b,x} = 1.58$ cm; $\sigma_{b,y} = 0.24$ cm
At slit SL-30	$\sigma_{b,x} = 0.79$ cm; $\sigma_{b,y} = 0.21$ cm
Maximum aperture opening	
Collimator	$b_x = b_y = 4$ cm
Slits SL-10 and SL-30	$b_x = 15$ cm ($\Delta p/p = 2.66\%$ and 5.13%, respectively)
Total length	30 radiation lengths
Total usable height	$\pm$7.5 cm
Materials	
Modules	Aluminum alloy 6061-T6 and water
Water piping	Stainless steel Type 316-L
Vacuum shells	Stainless steel Type 304-L
Maximum water pressure	75 psia
Water flow velocity in prime heat transfer areas	$\geq$150 cm/sec ($\approx$5 ft/sec)
Minimum flow rate	
For 2.2 MW	950 liter/min ($\approx$250 gal/min)
For 1 MW	750 liter/min ($\approx$200 gal/min)
Maximum water inlet temperature	40°C
Operational vacuum	$\leq 10^{-4}$ torr
The apertures are remotely adjustable during beam operation	

[a] See Reference 6.

some detail. Finally, some fabrication highlights are described and illustrated with photographs.

The high-power collimator (C-1) and A-beam slit (SL-10) are presently in operation. A high-power B-beam slit (SL-30) identical to SL-10 is planned for the future. The important criteria are summarized in Table 20-5.

Slit and collimator analysis

Until recently, accelerator powers and intensities were low enough to permit the use of almost any material and geometry. A collimator was simply a block of medium-Z or high-Z material containing a hole to fix the desired aperture. Similarly, the jaws of a slit consisted of two opposing blocks of such a material. The blocks formed a variable gap and were operated in a vice-like manner.

For multigigaelectron-volt, multimegawatt electron beams, entirely new concepts must be formulated and applied. At SLAC, various collimator concepts were analyzed.[24] It was demonstrated that a water-cooled, rotating-drum-type collimator was feasible in principle as an aluminum structure for up to 2.2-MW average beam power, at least on the basis of evaluation of heat transfer, thermal stress, strain, and fatigue problems. The same geometry, using OFHC copper as the material, could operate safely for average beam powers up to 500 kW. However, the rotating drum-type collimator presents some very difficult problems associated with the operation of bearings and dynamic seals in a vacuum under high radiation doses (up to 10^{14} ergs/g/yr are expected), and a nonrotating device has obvious advantages.

In a quasi-stationary slit, even medium-Z materials must be ruled out, since the thickness of power-absorbing walls becomes too small for practical applications. Walls cannot be made infinitely thin since they separate the vacuum system from the coolant under pressure, i.e., the device is a pressure vessel. The optimum geometry for a given pressure is a hollow circular cylinder, a tube. The feasibility of a modular array of tubes or a "tube forest" as the basic collimator element has been demonstrated.[12,25]

Efforts to fabricate prototype collimator elements of the tube-forest model were not fully successful. The multitude of water-to-vacuum joints presented problems. A modification of the tube-forest concept was, therefore, developed. The idea was to let the spacing for pump-out between the outside diameters of individual tubes in the array shrink to zero, i.e., to bring all tubes into physical contact with all adjacent tubes. A solid block of material, perforated with an array of holes having a diameter identical to the inside diameter of the tubes, closely approaches this concept as shown in Fig. 20-7. The number of water-to-vacuum joints in one plane is thus reduced to one at the periphery.

Figure 20-7 Geometric configuration of high-power slit modules.

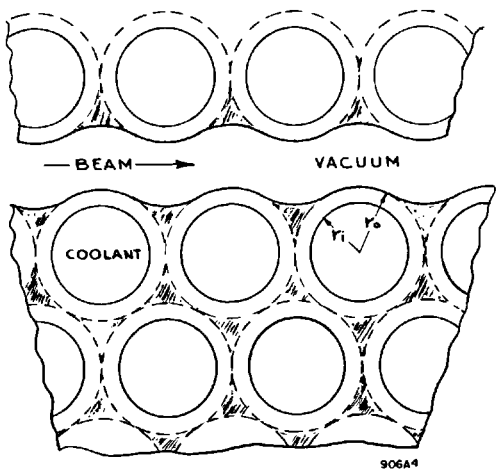

The heat transfer behavior of this new geometry is to first approximation still represented by the hollow circular cylinder geometry. For a wall thickness which is small in comparison to the particle beam size, one can assume uniform heat source distribution as a result of the beam power deposition. To first approximation, axial conduction can be neglected. The temperature distribution is described by Fourier's law of conduction. For steady-state, uniform heat source distribution, Eq. (20-8) may be written in polar coordinates as

$$\frac{d^2T}{dr^2} + \frac{1}{r}\frac{dT}{dr} + \frac{S}{k} = 0 \tag{20-17}$$

with boundary conditions

$$T(r_i) = T_i \tag{20-18a}$$

and

$$q'(r_i) = 2\pi k r_i \left(\frac{dT}{dr}\right)_{r_i} = \pi(r_0^2 - r_i^2)S \tag{20-18b}$$

where q' is the heat transfer rate per unit length across the metal–liquid interface.

The solution to this set of equations is

$$T = T_i + \frac{S}{2k} r_0^2 \ln\left(\frac{r}{r_i}\right) - \frac{S}{4k}(r^2 - r_i^2) \tag{20-19}$$

and the maximum temperature difference across the cylinder wall is

$$\Delta T = \frac{S}{4k}\left[2r_0^2 \ln\left(\frac{r_0}{r_i}\right) - (r_0^2 - r_i^2)\right] \tag{20-20}$$

The heat source S can either be calculated as outlined earlier or it can be extracted from curves such as given in Fig. 20-2. In order to make computational results realistic, an effective beam size has to be defined. Peak power dissipation occurs at the origin, $r = 0$. Values obtained in this fashion would, however, result in unrealistically high temperature gradients. Therefore, an "effective" beam size equal to the "hot core" of the beam is used. It was arbitrarily defined as the space limited by a radius, r_{hc}, at which the local power deposition is 80% of the peak value occurring at the origin. The power deposition is then averaged within this volume element and results in the value for the heat source. For the case of an incident beam of standard deviation $\sigma_b = 0.3$ cm, the corresponding value of the hot core at the shower maximum is $r_{hc} = 0.26$ cm. Knowledge of the radial power deposition distribution in just a few depth locations is sufficient to construct a curve expressing the relationship of the "percent of power" deposited (within r_{hc}) per unit

length versus shower depth. Heat source values can then be calculated readily by using curves given in Fig. 20-1 and multiplying each value obtained by the percentage value for that shower depth. It should be pointed out that this gives conservative values for the slit geometry under consideration, especially up to the shower maximum. This is due to the presence of large quantities of water with a significantly lower Z than aluminum. Moreover, there exists a strong dependence on σ_b at the beginning of the shower development. For increasing depth this factor becomes less important, and scattering and shower-spread dominate.

Note further that, for the case of the slit or collimator geometry, the Monte Carlo calculation for a semi-infinite solid gives excessive heat source values and, therefore, excessive temperatures. In this application the beam will always impinge close to the beam-defining edge, i.e., the system boundary. In that case, no infinite medium exists in the transverse direction. Shower particles will leave the boundary and are lost for further multiplication and power deposition in that area. It has been estimated[26] that this will reduce the power deposition values obtained for an infinite medium by at least a factor of 2. Once S has been determined, the temperature distribution and gradient can be calculated. The heat transfer rate per unit area at the metal–water interface is also readily obtained as

$$q''(r_i) = \frac{q'(r_i)}{2\pi r_i} = \frac{S}{2r_i}(r_0^2 - r_i^2) \tag{20-21}$$

The temperature distribution is slightly perturbed by the presence of heat sources in the triangular space formed by each three adjacent cylinders (see shaded areas in Fig. 20-7). An estimate of the peak temperature in that space can be obtained using Eq. (20-19) and redefining r_0. For a more accurate result an electrical analog would readily give the proper temperature distribution.

Finally, it should be mentioned that the temperature gradient as calculated from Eq. (20-20) gives somewhat excessive values, since it does not account for axial heat conduction. A more accurate value can be obtained from the following form of Eq. (20-8), assuming steady state and no circumferential heat source variation:

$$\frac{\partial^2 T}{\partial r^2} + \frac{1}{r}\frac{\partial T}{\partial r} + \frac{\partial^2 T}{\partial y^2} + \frac{S(y)}{k} = 0 \tag{20-22}$$

where y denotes the axial dimension. Equation (20-22) is a Poisson equation; $S(y)$ has, to first approximation, a Gaussian distribution and can be written as $S(y) = S_0 \exp[-y^2/2\sigma^2]$, where S_0 is the peak power density at the origin. The equation can be solved either by a Laplace transformation or by finite difference methods. Assuming $S(y)$ to be a step function allows a quick solution of the boundary value problem by separation of variables and superposition of results.

The maximum possible principal thermal stress in a fully restrained system due to a temperature gradient may be calculated from Eq. (20-12) using Eqs. (20-20) and (20-21),

$$\sigma_{th} = -E\alpha\,\Delta T_{tot} \tag{20-23}$$

where the effective temperature difference for the thermal stress development consists of two components,

$$\Delta T_{tot} = \Delta T_{film} + \Delta T_{metal} \tag{20-24}$$

Note, this stress is a compressive stress for a positive ΔT, i.e., a temperature increase.

Numerical example: Assume aluminum alloy 6061-T6 as material, $\Delta r = r_0 - r_i = 0.127$ cm ($=0.050$ in.), $\sigma_b = 0.3$ cm, $P_{AV} = 1$ MW. At a depth of 5 radiation lengths, one obtains from Fig. 20-1,

$$P' = 14.3\ \text{kW/cm}\left(= \int_0^\infty 2\pi r P(r)\,dr\right)$$

Approximately 9.5% of P' is deposited within the hot core for $r_{hc} = 0.26$ cm, thus $S = 6.4\ \text{kW/cm}^3$. Equations (20-20) and (20-21) yield $\Delta t = 35.5°\text{C}$ and $q'' = 0.88\ \text{kW/cm}^2$; if axial conduction is considered, Eq. (20-22), ΔT reduces to 32°C. Correction by a factor of 2 due to leakage of particles through the boundary yields a temperature gradient across the wall, from the vacuum to the water, of $\Delta T_{metal} = 16°\text{C}$ (or 35°C for $P_{AV} = 2.2$ MW).

Assuming a bulk water temperature of 40°C and a water pressure of 10 psig, $\Delta T_{film} \approx 74°\text{C}$. The effective total temperature gradient for thermal stress considerations, Eq. (20-24), is $\Delta T_{tot} = 90°\text{C}$, and the maximum metal temperature at the vacuum interface is 130°C. Equation (20-23) yields a thermal stress value of $\sigma_{th} = 22{,}500$ psi for a fully restrained system. The yield strength of alloy 6061-T6 at 135°C is $\sigma_{YT} = 30{,}000$ psi and the endurance limits for 10^6 and 10^{10} cycles are 18,000 and 12,000 psi, respectively. The instantaneous temperature rise due to 1 pulse is $\Delta T \approx 4°\text{C/pulse}$, which results in an additional cyclical thermal stress $\sigma_{alt\,max} = 1000$ psi. Superposition of the cyclical stress and steady-state stress can be accomplished by defining a mean effective stress σ_m as

$$\sigma_m = \tfrac{1}{2}(\sigma_{tot} + \sigma_{th}) = \tfrac{1}{2}(2\sigma_{th} + \sigma_{alt}) \tag{20-25}$$

For this example, $\sigma_m = 23{,}000$ psi. Next a Goodman diagram is constructed. Let the ordinate represent the cyclical stresses and mark $\sigma_E = 12{,}000$ psi for 10^{10} cycles. The abscissa is to represent the steady-state stresses and $\sigma_{YT} = 30{,}000$ psi is marked. The σ_E and σ_{YT} are connected by a straight line. The calculated sample point is located, with σ_{alt} as the ordinate value and σ_m as the abscissa value. Any combination of σ_m and σ_{alt} which results in a point located in the triangular area defined by the origin, σ_E, and σ_{YT} has unlimited life expectancy. For this example, i.e., $P_{AV} = 1$ MW, no fatigue failure is expected. It can also be shown that a 2.2-MW beam can be safely dissipated for $\sigma_b \geq 0.3$ cm.

Material selection and corrosion problems

An evaluation of low-Z fabrication materials resulted in selection of aluminum alloy 6061-T6 for the slit modules. This alloy has good corrosion resistance (as will be shown below), strength, and thermal conductivity. It has been successfully applied for uranium fuel element claddings in nuclear reactors where it experiences similar operating conditions. The strength–temperature relationship is flat and favorable up to 150°C.

For higher temperatures the strength decreases rapidly and small temperature changes result in large strength variations. Design in this region is not recommended unless one can pinpoint the temperature accurately. The alloy is quite immune to radiation-induced lattice structure changes for doses up to 10^{16} ergs/g. Formation of vacancies and interstices slightly increases the yield and ultimate tensile strength. For higher doses a rapid increase in strength is recorded; the material becomes brittle. Some of the alloying constituents are more likely to be displaced from their proper lattice site and chemical property changes in addition to mechanical ones may be of importance. The low-Z of the slit module materials also helps to keep down induced radioactivity, an important factor in accessibility to slit and collimator locations.

Stainless steel Type 316-L was selected for the water piping for reasons stated in the previous section. Important links in the water system are bellows which allow supply and return of water to the adjustable slit jaws. Inconel 600 was selected as the material for this application. It does not appear to be susceptible to stress-corrosion cracking and exhibits good all-around corrosion resistance. This is most important for stressed components with thin walls ($\approx$0.03 cm). Inconel 600 and stainless steel Type 316-L can readily be joined by TIG welding.

All external materials exposed to the beam switchyard atmosphere were carefully selected to withstand this environment. High levels of radioactivity near the power absorbers will result in ionization of the switchyard atmosphere. Oxygen and nitrogen ions will combine to form nitrogen oxides, which, in turn, will form nitric acid with the water vapor in the air. Significant amounts of HNO_3 are expected to be formed at high-power operation[27] according to

$$2H_2O + 2N_2 + 5O_2 \rightarrow 4HNO_3 \qquad (20\text{-}26)$$

One molecule of HNO_3 is formed for each 35 eV absorbed.[28] It has been estimated[29] that at full power operation, approximately 600 W are absorbed by the air in the entire beam switchyard. This results in formation of the equivalent of approximately 1 liter/day of commercial, 70% concentrated nitric acid. At this time it is still difficult to estimate for what percentage of the time one has to expect full power operation in the future. Moreover, the switchyard is not hermetically sealed, and significant amounts of air are exchanged in the course of normal daily atmospheric pressure changes. The switchyard air is also vented irregularly after an appropriate cooling-off

period for maintenance work. Nevertheless, the net amount of HNO_3 left might turn out to be significant and warrants careful selection of materials.

The slit and collimator vacuum shells, flanges, bellows, and other important structural items are fabricated from stainless steel Type 304-L. This material also exhibits less outgassing than mild steel, and pump-down time is shortened. The support structures are very massive, and the use of stainless steel would have been prohibitively expensive. They were fabricated instead from mild steel. Nitric acid corrosion is not expected to jeopardize seriously the proper functioning of these structures.

The usual rust layer formed on mild steel surfaces may, however, present a health hazard. The rust is continuously being irradiated as is the rest of the equipment, and induced radioactivity could make maintenance work dangerous. Radioactive rust particles could be picked up on shoes and clothing. The seriousness of radiation through the soles of the feet is seldom treated with sufficient concern. There is also the remote possibility that under dry conditions rust particles may become airborne and could be inhaled.

All support structures were, therefore, painted with a highly radiation-resistant, corrosion inhibiting paint. For highest resistance the paint has to be baked onto the surface. This operation was combined with a stress-relief operation to increase dimensional stability. Materials painted in this fashion have been exposed to a total dose of 2.4×10^{13} ergs/g. They showed no indications of damage, and adhesion was not impaired.[30]

A cause for concern was the simultaneous presence of aluminum and stainless steel in the slit and collimator radioactive water loops. Stainless steel is cathodic and aluminum with its high anodic potential reacts with most cathodic materials. A literature survey was carried out[31] on the corrosion behavior of aluminum alloys in a closed-loop aqueous system in the presence of stainless steel, nuclear radiation, varying water purity, temperature, and heat flux. Several corrosion mechanisms are active.

1. Aluminum reacts with oxygen-containing water by thermochemical or direct corrosion according to the equation

$$4Al + 3O_2 + 6H_2O \rightarrow 2Al_2O_3 \cdot 3H_2O \qquad (20\text{-}27)$$

This hydrous aluminum oxide is called "bayerite." It adheres well to the aluminum surface and is primarily responsible for the favorable corrosion behavior of aluminum. At elevated temperatures a denser oxide film is formed, $Al_2O_3 \cdot H_2O$, known as "boehmite." The solubility of bayerite in high-purity water[32] is a function of pH and is at a minimum at a pH of approximately 5. At this level of acidity, stainless steels suffer some attack.

2. The presence of cathodic materials, particularly copper, causes electrochemical corrosion. Copper ions in the aqueous system will plate out on the aluminum surface and they will cause pitting of the aluminum. Stainless steel and chromium result in only slight electrolytic attack unless in direct contact, even though both have a cathodic potential. No problem exists if high purity of the water is maintained.

3. Pitting corrosion or formation of little pits or cavities is brought about by a local cell action on a very small scale. Chemical (for example, copper ions) and geometrical discontinuities on the surface are responsible for local destruction of the passivating oxide film, followed by formation of a cell. High local currents and corrosion rates are the result. At elevated temperatures, above 100°C, pitting is not a serious problem.

4. Failures due to stress-corrosion have been encountered. High purity water and the use of certain tempered (heat-treated) aluminum alloys with a fine, random grain pattern are good protection against stress-corrosion.

5. The previously described cavitation erosion phenomenon associated with high heat transfer rates results in accelerated loss from the aluminum surface. This is partly due to increased solubility in the boiling heat transfer zones and partly due to spallation of the brittle oxide film.

6. Aluminum and most of its alloys react favorably with respect to corrosion while irradiated in aqueous systems.[33] Observations of lower corrosion rates than for unirradiated systems were made. The author believes that the difference in the corrosion behavior is due to formation of hydrogen peroxide and oxidizing free radicals in the radiolysis process in water. The oxidizing agents, in turn, will cause formation of an even denser protective oxide film on the aluminum surface which retards further corrosion.

Aluminum alloy 6061-T6 satisfied most of the fabrication, strength, fatigue and corrosion criteria and was selected as module material. Rigid control of water purity is essential for long-term operation. The water should be kept acidic; whereas a pH of 7 would favor the stainless steel, a pH of 5 would be preferable for the aluminum. The systems at SLAC show a pH of 6.2 to 6.5 and resistivity is better than 1 megohm-cm.

Finally, one should mention the transition from aluminum to stainless steel which exists in various locations. Commercially available brazed transition pieces were used. In that application, aluminum is in direct contact with stainless steel, except for the brazing material interface, and a potential hazard exists.

Design feature highlights

Both the collimator and the slit have variable aperture openings. The collimator is formed by placing two slits in series with the second rotated 90° with respect to the first about the common axis. A slit is 30 radiation lengths (≈ 5 meters) long, so each one had to be built up from modular sections for fabrication and alignment reasons. Typical modules are shown in Figs. 20-8 and 20-9.

A total of eleven modules are assembled to a strongback to form a jaw, and two opposing jaws form a slit. Figure 20-10 shows a partially completed horizontal slit. It is desirable to build these devices as short as possible since space is at a premium. The length can be optimized if the governing wall thickness between adjacent holes as well as the vacuum interface is tailored

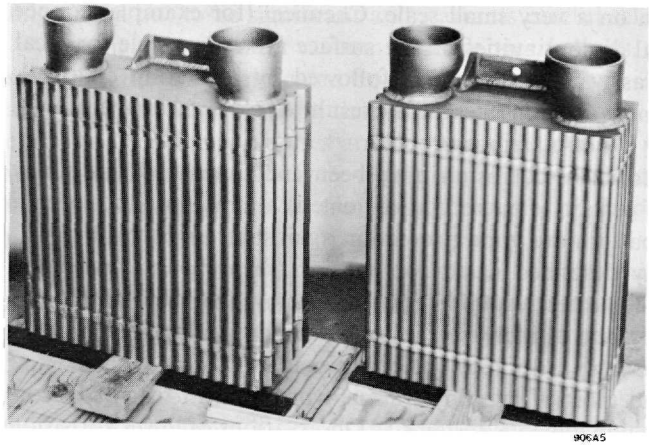

Figure 20-8 Front view of high-power slit modules.

according to shower development and attenuation. This was done for economical reasons in discrete steps rather than continuously. Thus, the ratio of aluminum to water and, therefore, the effective Z is increased downstream from the shower maximum in favor of aluminum according to shower attenuation.

Figure 20-9 Top view of slit modules.

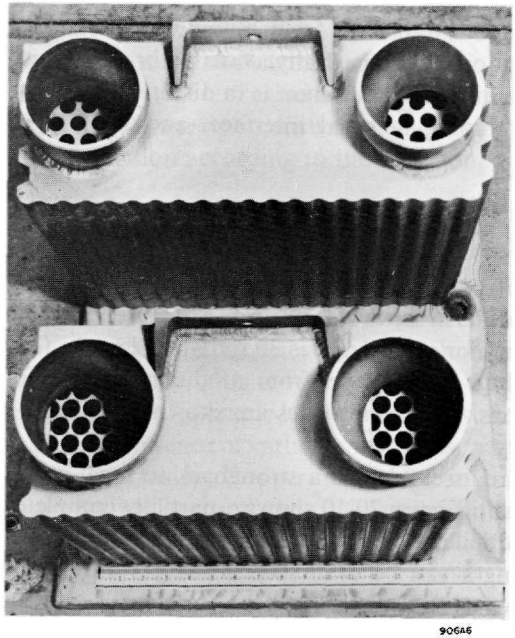

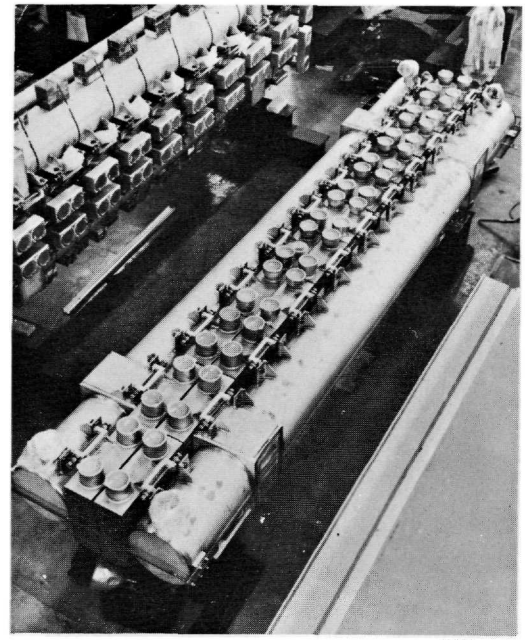

Figure 20-10 Horizontal slit module–strongback assembly (SL-10) with vertical slit assembly (C-1-V) in background.

Each module floats axially with respect to the strongback on linear ball bushings; this allows for thermal expansion between strongback and power-absorbing modules, and the strongback can properly maintain the straightness of the beam-defining edge. The strongback is fabricated from stainless steel Type 316-L as a hollow circular cylinder for maximum torsional rigidity. It is used as water inlet manifold and its temperature remains essentially constant during operation. Only the last module is rigidly connected to the strongback via the water inlet pipe and all modules are in series in the water loop.

A double pantograph assembly (parallelogram linkage) is used to provide center-line stability. The link between two opposing pantographs is made for zero backlash with high-strength, low-stretch aircraft cables, Fig. 20-11. Spherical ball-journals connect pantograph arms and strongback. They allow differential gap opening between front and back of the slit jaws which may be used to accommodate angular divergence of the beam. Proper assembly of two opposing jaws allows nesting of the module convolutions, i.e., no line-of-sight is possible, and a slit can be used as a beam stopper (for principle, see Fig. 20-7). In order to protect equipment downstream of the collimator or slit from excessive radiation and to minimize the possibility of halo (penumbra) formation behind the beam-defining edge due to the low-Z aluminum–water combination, a set of 9.5-radiation-length copper modules

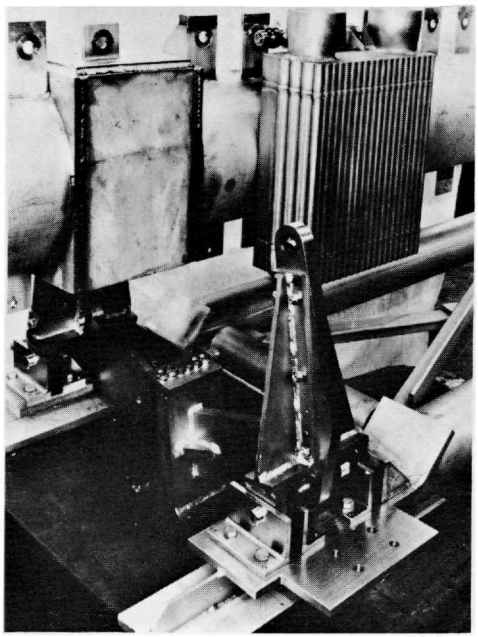

Figure 20-11 Strongback–pantograph assembly of high-power slit.

was installed. They are bolted to the last aluminum module and cooled by conduction only.

The completed slit assemblies were pneumatically pressure tested to 100 psig, using dry nitrogen. They were then placed in a vacuum tank, where they are operated by means of two actuators attached to the front and back of one jaw. The operating vacuum in the slit tank is approximately 10^{-5} torr. The assemblies were leak-checked with a helium mass spectrometer. No leaks were detected at the highest sensitivity of the instrument, 10^{-10} standard-cm^3 He/sec.

Thermocouples are connected to the copper blocks to monitor their temperature. Secondary-emission monitor foils are installed in front and back of each jaw. Figure 20-12 shows SEM foils attached to the front of a slit and the associated copper-jacketed, mineral-insulated (MgO) cables which serve to bring the signals out of the vacuum and radiation environment. The reason for the cable coils is to minimize bending stresses during aperture adjustments and, thus, to prevent fatigue failure. The SEM foils are used for protection of the jaws in front and for monitoring losses at the back. In the case of a slit they can be used for rough monitoring of drift in the momentum spectrum.[34] A more detailed description is presented in Chapter 19.

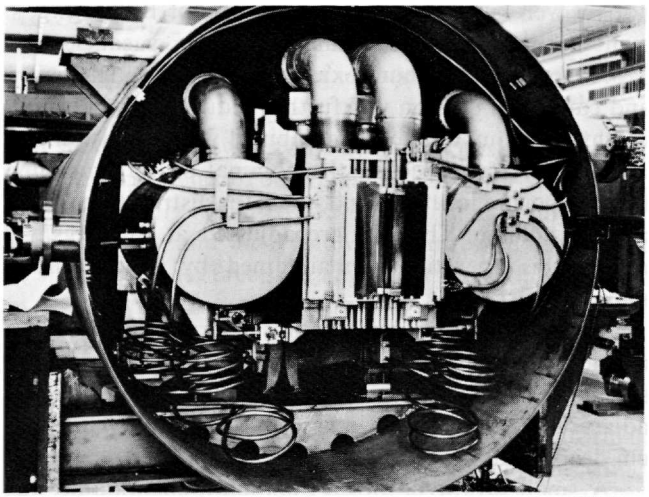

Figure 20-12 Front view of high-power slit (SL-10). Slit assembly placed in the vacuum tank, with secondary-emission monitor foils.

Modules and their fabrication

As already indicated above, eleven individual modular elements make up a slit jaw. The first six modules are identical and the water-to-vacuum wall thickness is $\Delta r = 0.127$ cm (0.050 in.). Note that for 20-GeV electrons the shower maximum occurs at the beginning of module No. 4. Modules No. 7 and 8 are identical and $\Delta r = 0.305$ cm (0.120 in.). Module No. 9 has $\Delta r = 0.760$ cm (0.300 in.), and the last two modules are again identical with $\Delta r = 1.520$ cm (0.600 in.).

The modules were manufactured from high-quality aluminum blocks which were forged, stress-relieved, and tempered to a T-6 condition. Each module consists of 3 parts: a 30-cm-high module body and two flow headers. The machining of 30-cm long holes of 1.6 cm diameter presented many difficult problems. Tolerances on hole position and parallelism had to be held very closely to satisfy temperature, Eq. (20-20), and corrosion criteria. Different techniques were investigated, including gun drilling, electric-discharge milling (EDM), and electrochemical milling (ECM). The problem was finally successfully solved with a tape-controlled, deep-hole drilling technique. The flow headers were welded to the module body with an electric arc (TIG) method for thin walls and with the electron beam welder for thick walls. Full penetration was required to minimize crevice corrosion and notch sensitivity problems. Total leak rates in excess of 10^{-9} standard-cm^3 He/sec were cause for rejection.

The reasons for the height and depth of the modules are as follows: radiation damage due to high-energy electrons penetrating the aluminum is

not yet well known. For doses in excess of 10^{16} ergs/g, significant embrittlement is known to result from dislocations, vacancies, and interstitial atoms. Moreover, the aluminum oxide film may spall in the area of high heat flux, and cavitation erosion will further reduce the wall thickness. An increase in height of the module body combined with provision for vertical adjustment of the slit with respect to the nominal beam center line allows for various beam exposure locations and, thus, for distribution of the radiation dose over a large volume. The slits are adjusted at 10^{10} ergs/g. Center-line stability during this operation is maintained by two guideposts mounted on the main support frame.

The module transverse depth is determined by radial shower development considerations, maximum transverse beam excursion, and beam momentum spread. A maximum transverse flux of 1 W/cm^2 leaving the module plane adjacent to the strongback was set as criterion. The modules were made 16.5 cm deep to satisfy this condition.

A small prototype of an aluminum slit module was tested for thermal shock[17] in the Astron accelerator at Lawrence Radiation Laboratory in Livermore. This high-intensity machine can produce bursts of very high power density over short periods of time. The peak power density was achieved by a beam of $E_0 = 3.8$ MeV, $I_{peak} = 90$A, pulse length $= 0.3 \times 10^{-6}$ sec, pulse repetition rate = 5 pulses/sec, and beam diameter = 1 cm. The resulting local heat flux is low compared to the design criterion. Much more spectacular is the rate of energy deposition during the pulse, which gives rise to very steep temperature gradients in space and time, resulting in proportional thermal stress gradients. For this run the rate of energy deposition during the pulse in the module wall was 600,000 kW/cm^3. Although very high in comparison with such values from other accelerators, this power deposition was not high enough to damage the aluminum. No effect on the module wall was visually detectable after several hours of beam exposure. Thus, even for a well-focused SLAC beam, no thermal shock and spallation problems (beyond spallation of oxide films) are expected for the high-power slit and collimator.

Fabrication and alignment

The slits were assembled in the SLAC fabrication facilities. The internal slit assemblies were built in a clean room, using methods which are considered good practice for handling of vacuum equipment. Particular attention was focused on the alignment of the beam-defining plane formed by the convoluted face of all the modules. The latter were optically aligned flat to ± 0.015 cm. As was mentioned earlier, the dispersion at the slit due to the first bending magnet group is 0.15%/cm. The completed slit assembly was tested for alignment hysteresis under vacuum. Hysteresis up to 0.013 cm was recorded.

The horizontal and vertical slits of the collimator are tied to laser beam stations. The relationship between the slit center line and the laser beam center line was established in the shop. A Fresnel target allows positioning of

the slit such that its center line coincides with the nominal electron beam center line. This is discussed in more detail in Chapter 22.

Assurance concerning the actual location of each slit and its center line is obtained in three different ways:

1. Second level optical survey in the switchyard is used to position each slit with respect to an external reference. Tooling balls and mirror stages (see, for example, Fig. 20-13), rigidly mounted to the external structure of the slit, were set during assembly and have known distances and rotations with respect to the slit center line. Precision alignment jacks allow adjustments to 0.003 cm accuracy.
2. The two slits of the collimator (as well as the high-Z collimator) are connected to laser beam target stations as described above. A laser survey can detect deviations of 0.001 cm.
3. The electron beam can be used as a survey tool to ascertain such information as rotation of the slit about an axis normal to the beam center line and comparison of center-line location of high-Z and high-power collimators or slits. This information is obtained using two steering magnets to deflect the beam across the front face of the slit. The beam current transmission is then measured as a function of magnet current. Differences of 0.005 cm can be detected.

Figure 20-13 High-Z collimator (C-0) with high-power collimator (horizontal slit C-1-H) as installed in the beam switchyard.

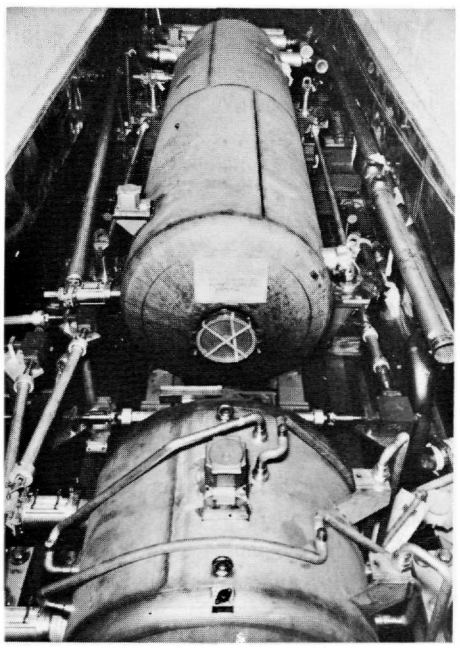

Operations to date

Although power levels encountered to date (July 1967) have been low, operations of high-power slits and collimators for the first 12 months have been essentially faultless. Up to approximately 50 kW of average beam power has been dissipated. Reproducibility of aperture width and center line of a 5-meter long slit of ± 0.03 cm has been achieved.

The primary radioactive water system is similar to the one for the high-power beam dump and will not be discussed in further detail. Hydrogen recombiners are planned for installation in the near future.

The question of whether or not the low-Z and large physical length of these slits have a negative effect on beam analysis and definition has not yet been investigated. However, the limited number of physics experiments conducted so far has not uncovered any deleterious effects.

20-6 High-Z slits and collimators (WSS, DRW)

Variable-aperture, low-power, high-Z slits and collimators were designed and built to serve as backup devices for the high-power units. The slit material is copper and properly only medium Z, but the term "high Z" was used to distinguish these devices from the high-power units described in the previous section. Two collimators and two slits are now in use: a collimator (C-0) immediately upstream of the high-power collimator (C-1), a photon beam

Table 20-6 High-Z collimator and slit criteria

Maximum average beam power	
For minimum beam size, $\sigma_b < 0.3$ cm	20 kW
For average expected beam size, $\sigma_b \geq 0.3$ cm	40 kW
Incident beam energy	$\leq$25 GeV
Pulse repetition rate	1–360 pulses/sec
Beam sizes (see Table 20-5)	
Maximum aperture opening	$b_x = 15.0$ cm
Total length	35 radiation lengths
Materials	
Modules	OFHC copper
Water piping	Everdur 1015, stainless steel Type 316-L
Vacuum shells	Stainless steel Type 304-L
Maximum water pressure	175 psia
Water flow velocity in prime heat transfer areas	$\geq$150 cm/sec ($\approx$5 ft/sec)
Minimum flow rate for full power	34 liter/sec ($\approx$10 gal/min)
Maximum water inlet temperature	40°C
Maximum temperature rise	$\approx$25°C
Operational vacuum	10^{-4} torr or better
Aperture is remotely adjustable during beam operation	

collimator (C-10), and two slits (SL-11, SL-31) for momentum definition in the two beams serving the major research areas. The important criteria are summarized in Table 20-6.

Design features

The high-Z collimator and photon beam collimator (which are in most aspects identical) are formed, as is the high-power collimator, by two slits in series with the second rotated 90° with respect to the first about the common axis. Both the horizontal and vertical slits of a collimator are installed in one vacuum tank because of their small physical size. Two opposing OFHC copper modules form a slit. Figure 20-14 pictures a set of modules for the collimator (C-0). They are 10 cm deep, 20 cm high, and 50 cm long. The volume close to the beam-defining edge is perforated with a row of hole pairs for proper cooling. The water passages are connected in series by means of square flow cavities milled into the copper and closed with a cover plate braced to the module. The cavity reverses the flow direction and promotes good mixing. The minimum wall thickness between the collimating surface and the flow passages is 1.0 cm. The length of the modules is thus 35 radiation lengths up to a transverse depth of 1.0 cm, and it decreases to a minimum of 15.5 radiation lengths at a depth of 1.8 cm, coinciding with the centers of the first row of holes. In order to minimize the possibility of penumbra formation in the case of the slits and the photon beam collimator, the flow channels were altered downstream from the shower maximum. At an axial shower depth such that power deposition has decreased to a low level, the two parallel flow

Figure 20-14 High-Z slit copper modules before furnace brazing.

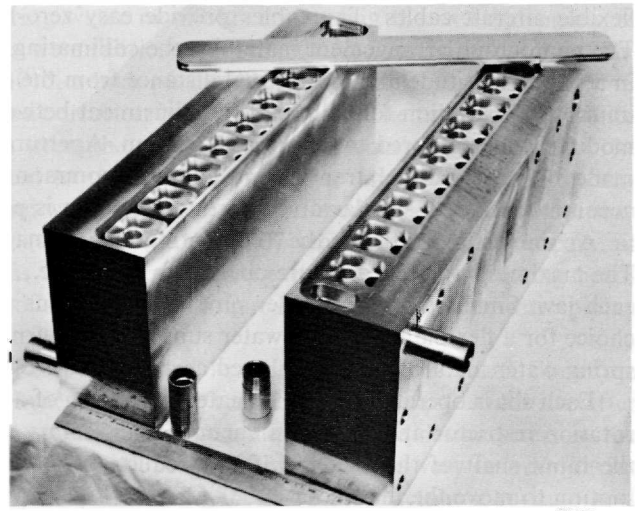

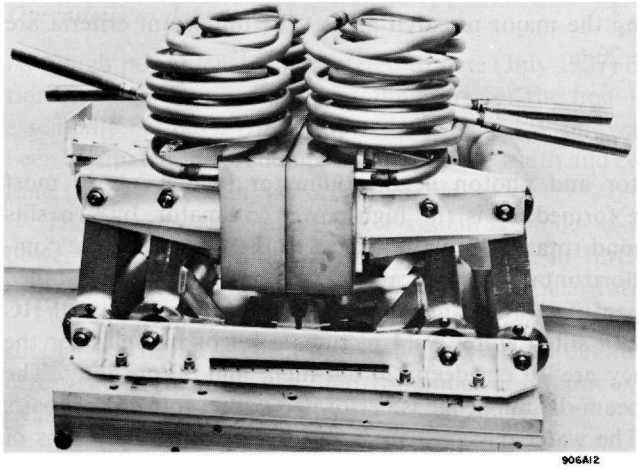

Figure 20-15 Double pantograph assembly with slit modules attached.

passages were combined into one, which is of somewhat larger diameter to keep the velocity constant. Its center is located midway between the two smaller passages. This provides an increase in Z downstream from the shower maximum in the transverse region extending from 1.0 cm to the flow passages.

The modules are mounted to a four-pivot point or double pantograph assembly as illustrated in Fig. 20-15. The pivot points are mounted on tapered roller bearings to allow adjustment for zero backlash. The two halves of the pantograph assembly are cross-connected with low-stretch, high-strength, flexible aircraft cables. The cables provide easy zero-backlash adjustment. The pantograph arrangement maintains the collimating faces of the modules in a parallel attitude and at an equal distance from the center line. The maximum total variation for full aperture adjustment between any two opposing modules was measured to be about 0.006 cm. Aperture adjustments can be made only as parallel translations about a common center line, i.e., no accommodation to angular divergence of the beam is possible.

An interesting feature is the "coil-spring" water manifold, see Fig. 20-16. The maximum possible aperture opening is 15 cm, i.e., 7.5 cm translation for each jaw. Small stroke and other physical limitations make bellows a poor choice for a flexible link in the water supply and return lines. Thus, the coil-spring water manifold was developed as an alternative to bellows.

Each slit is operated by one actuator consisting of a precision jack with a rotation restrictor and a bellows vacuum seal. Rotary motion is supplied to the input shaft of the jack for 100 : 1 reduction and creation of the linear motion to move the modules.

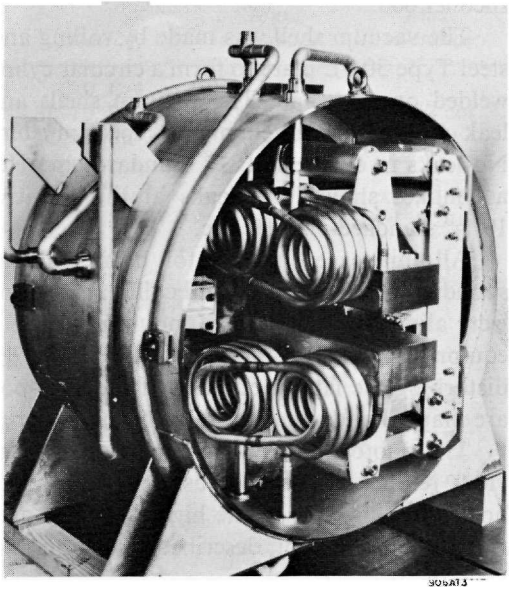

Figure 20-16 High-Z collimator (C-1, C-10); vacuum tank installation with view of "coil-spring" water manifold.

Fabrication and material selection

The modules were machined from solid forgings. To assure soundness in the furnace-brazed joints and prevent hydrogen blistering, OFHC copper was selected. The coil-spring water manifolds connecting the external piping to the movable modules were fabricated from extruded electrical conduit. The material is Everdur 1015, a high-purity silicon bronze. It was selected for its high strength and good corrosion behavior in water. The tube work-hardened and achieved its high strength and elasticity in the coil-bending process. The coils were hand-brazed to the module to confine annealing to the brazing joint. After all brazing was completed, the coil-module assemblies were shot peened with small glass beads (0.002–0.007 cm) propelled by 60 psig air pressure. Brazed areas received prolonged exposure to the impinging beads to assure restoration of strength and fatigue life. The rest of the water piping is stainless steel, Type 316-L.

The pantographs were fabricated as welded structures from aluminum alloy 6061, solution heat-treated and tempered to the T-6 condition after welding. To maintain stability the maximum allowable design stress in the pantograph assembly was set at 3500 psi. This compares very favorably with a yield strength of 40,000 psi for alloy 6061-T6. The actuator vacuum seal

bellows are of the welded diaphragm type, fabricated from 0.015-cm thick Inconel 600.

The vacuum shell was made by rolling and welding 0.8-cm thick stainless steel Type 304-L plate to form a circular cylindrical vessel. Dished heads were welded on each end. The vacuum shells and slit assemblies were vacuum leak checked with a helium mass spectrometer at various stages of fabrication. No leaks in excess of 10^{-8} standard-cm^3 He/sec were allowed and all final assemblies showed no leaks at the sensitivity limit of the spectrometer, 10^{-10} standard-cm^3 He/sec.

All units except the photon beam collimator are mounted on the corresponding high-power slit and collimator support frames; see Fig. 20-13. They were aligned at the time of mounting to be coincident with the high-power equipment. Small lateral adjustments of ± 2.5 cm can be made without disturbing the lateral position of the high-power devices. These adjustments are manual and semiremote from the upper tunnel housing.

The photon beam collimator was installed on a special frame that provides remote powered adjustment of ± 3.75 cm in both the vertical and horizontal directions. The high-Z devices are tied into the magnet cooling-water (LCW) system, described in Chapter 24.

Operational experience

Functioning of all the high-Z units has been faultless to date (July 1967). The significant difference between the Z of the "high-power" and "high-Z" slits as well as a large difference in physical length (10 : 1) should make it possible to partially answer questions concerning the influence of these parameters on slit scattering and beam halo formation.

Magnets were used to deflect the beam across the front of the partially opened high-Z B-beam slit (SL-31) and beam current transmission was measured as a function of magnet current in order to obtain beam spectra. Figure 8-17 shows the spectrum for a 6 GeV beam (obtained on February 1, 1967).

20-7 Collimator actuation and drive system (LRL, DRW)

Two types of adjustments can be made on each slit and collimator: (1) remotely controlled motorized adjustments during beam operation, such as opening and closing the slit aperture, changing the collimator aperture, or changing the beam exposure location on the modules; and (2) semiremote and manual adjustments on maintenance days, performed in the tunnel housing —this covers all alignment operations and is done solely by mechanical precision jacks.

In case of a major disturbance, such as a severe earthquake, it is possible to add or remove spacers up to ± 15 cm. Table 20-7 summarizes the important criteria with identification of individual equipment.

All remotely controlled adjustments are accomplished from the Data Assembly Building (DAB). A group of panels in the DAB houses the

Table 20-7 Actuation and alignment system criteria

Variables	*Device*	*Max. translation*	*Max. tolerance*
Gross manual positioning of support frames, transverse to the beam direction	C-0, C-1 SL-10, SL-11 SL-30, SL-31	±15 cm	±0.3 cm
Semiremote, manual alignment of support frames transverse to the beam direction	C-0, C-1 SL-10, SL-11 SL-30, SL-31	±7.5 cm	±0.05 cm
Semiremote, manual alignment of high-Z support frames in horizontal plane	C-0 SL-11 SL-31	±2.5 cm	±0.010 cm
Maximum possible aperture opening (remotely, motorized)	C-0 SL-10, SL-11 C-10 C-1	15 cm 3.8 cm	
Reproducibility of aperture and center line (including all tolerances)	All Devices		±0.06 cm
Remote, motorized alignment of photon beam collimator support frame	C-10	±3.75 cm	±0.005 cm
Remote, motorized change of beam exposure location (radiation damage distribution)	C-1 SL-10 SL-30	±7.5 cm	±0.15 cm
Maximum allowable time for aperture adjustment for all devices		1 min	
Minimum ambient temperature range capability of equipment		20°–60°C	
Radiation dose expected in close vicinity of high-power devices for full power operation		10^{12}–10^{13} ergs/g/yr	
Atmosphere may contain varying amounts of HNO_3			

controls, readouts, and warning lights. The system is built to be controlled and operated by the SDS-925 computer. This interface of the actuation system is discussed in detail in Chapter 19.

A typical remote-controlled, motorized actuation system comprises the following major components:

1. The electric and electronic interface with the DAB
2. The drive control box containing the prime mover, electromagnetic clutches, shaft encoders, potentiometers, and limit switches
3. The drive train made up of shafts, universal joints, and angle gear boxes (miter gears)
4. The actuator in the form of a precision jack to transform rotary into linear motion.

A typical alignment point is simply a precision jack coupled to an angle gear box for easier adjustment from the upper tunnel of the switchyard housing.

The prime mover and control box

The prime mover for each type of motorized drive system is an ordinary electric gearmotor. The motor and the associated equipment are contained in a partially sealed box in a wall chase in the upper tunnel of the switchyard housing. This location was selected for easy maintenance access and because the radiation levels are two orders of magnitude lower than in the close vicinity of the energy absorbers; the expected dose rate for full power operation is then 10^{10}–10^{11} ergs/g/yr. All the components in the box are of usual materials with normal lubrication. The control box can be flooded with dry instrument air if moisture or nitric acid becomes a problem.

The motor and associated equipment are operated remotely from the DAB, either manually or by computer. In the case of a jaw drive for aperture adjustments either high-speed or low-speed operation is possible. High-speed operation is necessary to satisfy the 1-min criterion for full aperture adjustment. Low-speed operation allows achievement of close tolerances. The usual aperture adjustment procedure is first high-speed operation for fast approach to the vicinity of the desired aperture and then low-speed operation for accurate adjustment. The rate of aperture change of the high-power slit (SL-10), for example, is 0.016 cm/sec for low speed and 9 times faster, or 0.148 cm/sec, for high-speed operation. The front and the rear ends of the high-power slit jaws may be driven independently or in unison.

Figure 20-17 shows a typical drive box with the cover removed. The gearmotor located in the upper-right-hand corner drives a central shaft. This shaft terminates at the high-speed electric clutch. Directly below is the low-speed clutch. The electric clutches at the upper end of the left or right drive output shaft can engage either or both shafts. To the left of each output shaft is the counter shaft. It is coupled on the top to a gray bit shaft encoder and on the bottom to a mechanical counter for local reference. The encoder makes one revolution for the full opening of the slit aperture and gives 1024 counts. Table 20-8 gives a summary of this information. To the right of each output shaft is a threaded shaft that operates the limit switches and also drives a ten-turn potentiometer for a crude aperture opening display in the DAB.

The drive train

The output shaft of a control box is connected to the appropriate actuator, located in some instances 12 meters away, by a combination of drive shafts, miter gear boxes, and universal joints. The fact that rotary motion of the output shaft has to be transmitted around several corners and transformed

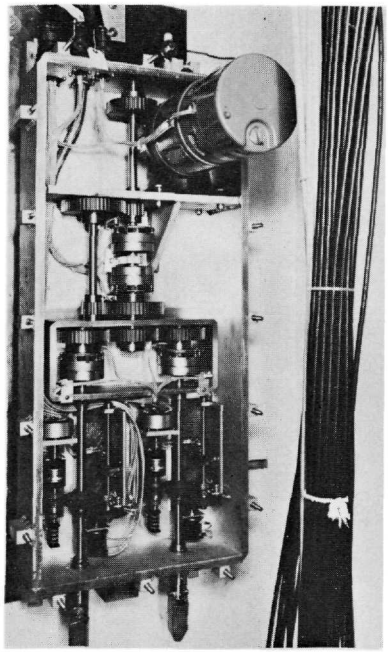

Figure 20-17 Aperture adjustment drive box.

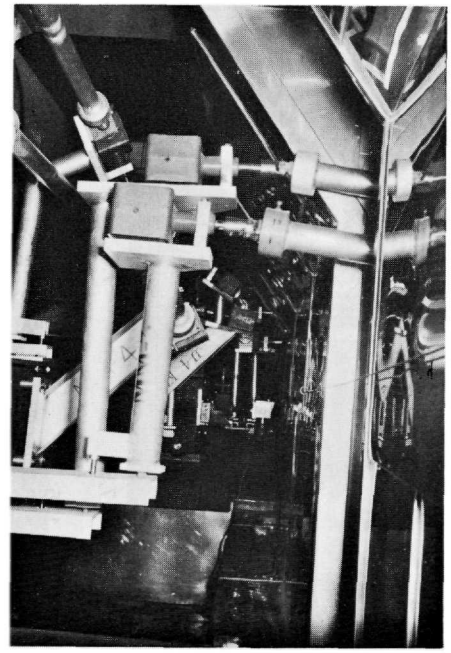

Figure 20-18 Slit, drive train, angle gear boxes and shaft disconnects.

into a linear motion at the slit with a minimum amount of backlash presented some interesting engineering design problems. The allowed accuracy tolerance was the equivalent of 0.005 cm of aperture width or 0.0025 cm of jaw position. The actuator jacks translate each input turn into a linear motion of 0.025 cm. Thus 0.0025 cm output is equivalent to 36° of shaft backlash. The actual shafting backlash achieved is about one-tenth of this figure.

The above problem becomes more complicated with the superposition of the slit tank motion requirements due to alignment and radiation-damage distribution criteria as given in Table 20-7. Figure 20-18 shows the typical solution. Most drive trains include two miter gear boxes but the solution is good for any number of boxes, provided that every second box is pivotally mounted as is the box in the center of the picture. The gear box is rigidly mounted on a stand. The stand can pivot about a pin located at its foot, and an outboard pin fitting in a slotted hole acts as a torque reaction arm. A universal joint is required on each side of the box. The remaining problem is, then, only one of geometry so that each shaft in the limits of its excursion clears the other shafts and equipment; see, for example, Fig. 20-19.

The universal joint ordinarily has one end bored and keyed to attach to a gear box. The other end is a square plug that inserts into the hub of the

Table 20-8 Slit and collimator drive system data

Characteristics	*Horizontal slit of collimator (C-1-H)*	*Vertical slit of collimator (C-1-V)*	*High power A-beam slit (SL-10)*	*All high-Z devices (C-0, SL-11, SL-31, C-10)*	*Photon beam collimator (C-10) support frame*
Maximum jaw travel ($\frac{1}{2}$ full aperture) (cm)	1.9	1.9	7.5	7.5	$x = 7.5$, $y = 7.5$
Drive box output					
Fast (rpm)	175	175	175	175	175
Slow (rpm)	19.5	19.5	19.5	19.5	19.5
Total output turns	75	57	300	327	300
Full-range total turns					
Encoder	1.0	1.0	1.0	1.0	1.0
Counter	150	150	150	150	150
Least count (per jaw)					
Encoder (cm)	0.0018	0.0018	0.0074	0.0074	0.0074
Counter (cm)	0.002	0.002	0.010	0.010	0.010
Full range adjustment time					
Fast (sec)	25.7	19.5	103	112	—
Slow (sec)	231	175	926	1010	926
Aperture closure rate					
Fast (cm/sec)	0.148	0.195	0.148	0.136	—
Slow (cm/sec)	0.0162	0.0217	0.0162	0.0152	0.0162

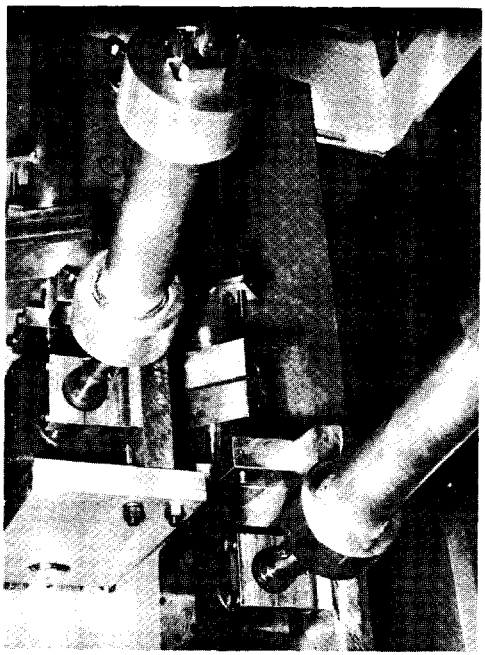

Figure 20-19 Slit drive train components (shafts, universal joints, angle gear boxes).

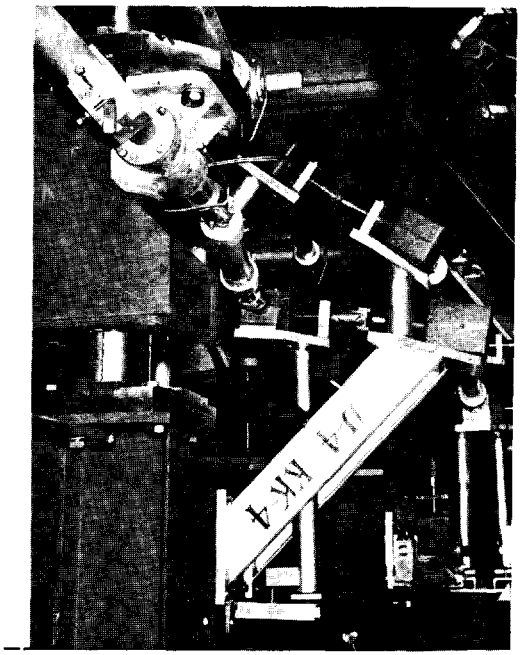

Figure 20-20 Guidepost, support jack and drive train for high-power collimator.

connecting shaft; see Fig. 20-20 at the top of the picture. The insertion depth is determined by a projecting pin on the side of the square and the shaft is retained by a screw bearing across the corner of the square.

In some instances the drive unit at each end of a drive shaft is fixed in location such as between jacks for radiation damage distribution, or between the drive box on the wall and the gear box below and on the same wall. In these applications the shafts are attached at one end with a universal joint, and the other end uses a T-slot termination; see Fig. 20-20 in the middle of the picture. The T-slot may be slid out of engagement after the keeper pin is pulled. Assembly and disassembly of drive train components can be done semiremotely from the upper tunnel housing.

The actuator

A commercial screw jack would be ideal for this service if it could be demonstrated that the mechanism would not jam after the lubricant has deteriorated due to radiation damage. Dose rates of 10^{13} ergs/g/yr are expected near the actuators for full power operation. This is too high for organic lubricants. However, historically accelerators do not operate at full power for the first

year or longer, and in the early stages they are not operated continuously either. Under these conditions a radiation-resistant organic lubricant might last for 6 months, 1 yr, or even longer. Radiation-resistant organic lubricants were irradiated at SLAC[30] with 5-Mev electrons. A polyphenyl ether appeared to be useful for switchyard applications for doses up to 10^{12} ergs/g. Its basic chemical structure is the benzene ring, known to be highly radiation resistant. This lubricant was used in applications where there was sufficient operating moment to shear through the polymerized resinous residue left by the decomposition of polyphenyl ether due to radiation.

Jamming is a combined geometry and lubrication problem. This is true for both rotary machinery and linear devices. A common trick for rotary machinery is, as in the case of the pivot wheel of a watch, to reduce the radius of the bearing to a point. The frictional moment, i.e., force times lever arm, is essentially zero even for high frictions because the lever arm is nearly zero. Unfortunately, for appreciable loads one has to have big bearings and the operating force must be applied at a large radius to prevent self-locking or jamming. Thus, designs for unlubricated applications become extremely bulky.

With these ideas in mind, a commercial jack actuator was modified and tested under various operating conditions. Leaded tin bronze is commercially available to fabricate unlubricated bearings. The jack worm gear was thus made of 10% leaded bronze. This gives control of the friction between the worm and the worm gear, and between the worm gear and the screw. The existing tapered roller bearings were replaced by ball bearings with a leaded bronze ball retainer. A leaded bronze retainer was also added to the thrust bearings. This modified jack operated, then, with input torques 1–3 times that of the normal lubricated jack for a life equal to at least 1 yr of service for the slit application.

The tests proved that the jacks would not suddenly become inoperative when the polyphenyl ether had polymerized. The wear of unlubricated jacks was very severe and it emphasized that the jack should be operated with a lubricant as long as possible. Up to date (July 1967), no jack has failed and all jacks are lubricated with polyphenyl ether. Since the leaded bronze is not resistant to nitric acid, each jack has a connector for admitting dry compressed air in case HNO_3 should become a problem.

Reproducibility

The aperture opening and center-line position are quite critical, particularly in the case of a momentum-defining slit. The drive should be as reproducible as possible. Momentum resolution is desirable to an accuracy of $\pm 0.01\%$ $\Delta p/p$ which amounts to approximately 0.062 cm (A-beam slit, SL-10). This rather generous figure disappears rapidly when all the contributing elements are added. Table 20-9 lists measurements for a high-power slit. One should note that the figures do not include any survey error.

Table 20-9 High-power slit tolerance and reproducibility data

Variables	*Tolerances (cm)*
Looseness of pivot joints in tank	$\leq$0.020
Jack output antibacklash	$\leq$0.005
Jack input (equivalent output backlash)	$\leq$0.010
Encoder least count	0.0075
Drive train backlash	$\leq$0.0025
Tank guidepost clearance	0.010
Frame adjustment ways	0.0075
Frame lateral jack backlash	$\leq$0.005
Lateral jack mount	$\leq$0.010
Total	0.0775

It may seem ridiculous to allow only 0.0025 cm of equivalent jaw error for a drive train from the tunnel below to the drive box in the upper tunnel housing and then at the same time give away 0.010 cm for a simple sliding pair such as the tank guidepost, seen, for example, in the left center of Fig. 20-20. However, the decisions are valid, and will be discussed in more detail directly below.

Dry friction and wear of materials

As has been pointed out above, situations can occur where rolling or sliding parts have to operate in a high-radiation environment containing varying amounts of nitric acid. Experiments were conducted at SLAC[17] to evaluate promising material pairs. The goal was to find corrosion resistant materials that can slide and roll dry, unlubricated, at minimum clearances, without galling or seizing and which show minimum wear. The vital part of the experimental apparatus consisted of a 3.75-cm diameter shaft rotating under 80-lb load in a 3.75-cm long sleeve bearing at 8 rpm. All experiments were conducted in air and at room temperature and were to establish minimum operating clearances.

Selection of material pairs was according to known friction and wear criteria. Dry friction always causes wear, but hard materials wear less than soft ones. Materials should have high moduli of elasticity, high recrystallization temperature, and resistance to plastic flow in order to minimize galling and seizing. A hardness of at least Rockwell C-42 appears to be required. Furthermore, a lamellar structure as found in dry lubricants such as molybdenum and tungsten disulfides and diselenides, graphite, and others is desirable. Slip between low shear strength layers causes formation of lamellar particles, and a hexagonal lattice structure has just this property. The selection

of materials was considerably aided by a recent book.[35] The concept that the equilibrium surface roughness and the wear particle size of a sliding or rolling pair is related to the surface energies of the two materials divided by the surface hardness is extremely useful where it is necessary to hold close tolerances. It is also shown that hexagonal lattice structure metals apparently did not have coefficients of friction higher than 0.6.

Attention was focused on finding and evaluating corrosion resistant, high strength materials having hexagonal lattice structure. Cobalt and titanium alloys performed remarkably well. Stainless steel 440-C hardened to Rockwell C-56, although not of hexagonal structure, made an excellent compatible material with the α-titanium alloy, Ti–5Al–2.5Sn. Stainless steel 440-C and Stellite No. 6 (Co-28 Cr-4W) also formed a very good material pair. Moreover, the experiments have shown that for these hexagonal materials it is not necessary to have dissimilar materials in the pair. Material pairs where both the shaft and the sleeve bearing were composed of stainless steel 440-C, Stellite No. 6 or α-titanium alloy (Ti–5Al–2.5Sn) performed very well. A selected material pair was considered a success if it survived 10^4 cycles without seizing for clearances <0.006 cm. Successful operations with clearances as low as 0.0018 cm were achieved. In contrast, 300 series stainless steels will fail with any practical clearance. For compatible materials, the minimum clearance is determined by the size of the wear particles and equilibrium surface roughness. If a material pair is compatible, it will establish its own characteristic equilibrium surface roughness regardless of the initial surface finish of each individual material. Having thus established compatible material pairs, dry lubricants can be used to lower the coefficient of friction, depending on application. But because of the thinness of dry lubricant films they cannot be relied on for successful operation; they are just an added bonus. The nonwelding properties of hexagonal lattice metals as found above have meanwhile been confirmed.[36]

Material selection

The materials for the drive system components were chosen according to preceding considerations and also according to price, delivery, and commercial availability.

For these reasons the gear boxes were of commercial cast steel frame. The shafts and gears were stainless steel and the bearings were graphite bushings. The graphite bushings require no lubrication; the moisture in the atmosphere is sufficient to keep the coefficient of friction low and the wear reasonable.

The stainless steel miter gear operating against another stainless steel gear was recognized as a poor choice, but delivery and manufacturing costs dictated this compromise. The gear teeth are lubricated with spray-on molybdenum disulfide. Replacements in the future should be a titanium gear against a stainless steel gear.

The universal joints were made of stainless steel with titanium pins and washers so rotating pairs are always stainless steel against titanium. Clearances are 0.012–0.028 cm.

Bearings and friction surfaces within the vacuum shells were surface coated with a low-coefficient of friction layer of tungsten disulfide. The latter was sprayed onto the surface at very high velocities. To date no wear failures or seizures have occurred in the slit and collimator drive system.

20-8 Protection collimators (AHK, DRW)

Protection philosophy and beam transport system problems

The many sizes of apertures through the beam transport system components in the BSY have resulted in a vacuum envelope of rather complex geometry. This fact, coupled with the high-power density characteristics of the accelerator, required that considerable attention be given to the possibility of damage to these components and the vacuum pipes resulting from excessive power deposition or excessive exposure to primary radiation. A protection scheme was developed[34,37] to minimize the probability of serious damage to transport components. It utilizes water-cooled, fixed-aperture protection collimators, ionization chambers, temperature sensors, and threshold current monitors strategically located throughout the BSY. All are interlocked to shut off the accelerator should the local beam losses or local temperature rises exceed predetermined levels or should the total beam loss reach an intolerable level.

There are several operating conditions in which primary beam or radiation can reach the vacuum envelope and beam transport components on either a continuous or transient basis. The most significant source of continuous power deposition in this equipment is due to the presence of particles of unwanted momenta in the spectrum of the beam. If the maximum deviation from a nominal momentum in the A-beam and B-beam transport systems were $\pm 1.3\%$ and $\pm 2.6\%$, respectively, the electrons would pass through the BSY (for slits open) without any power deposition at all. Unfortunately, the beam always has, to varying degrees, low and high momentum tails which become progressively more dispersed as the beam passes through the BSY bending magnets. The amount of power associated with these tails at any time depends on the operating conditions of the accelerator.

When the jaws of the high-power collimator and slits are intercepting the beam, radiation emanates from them and, hence, represents another source of continuous power deposition. Much of this radiation can reach components or vacuum chambers downstream, either because of a large angle of divergence or because of dispersion by bending magnets. An attempt[37] was made to estimate the amount of radiation emitted from the collimator (C-1) during transmission of a high-power beam. For the case of a 20-GeV, 2-MW average power beam, assumed to have a uniform power density to a radius $r_b = 0.3$ cm,

and the center of which is coincident with the edge of one of the aluminum jaws of the collimator, the following estimates were arrived at:

1. Most of the cascade shower particles re-entering the vacuum envelope are of rather high momentum with less than 10% having momenta below 2.5 GeV/c.
2. Leakage out of the jaw in the form of electrons and positrons amounts to 24 kW, and a leakage of 16 kW is due to photons
3. The power figures are order of magnitude but probably low due to the effective low-Z of the aluminum–water composition of the slit modules
4. Further, the power figures are low because the number of particles to be considered will increase with small misalignments and distortions, and they are also low because for a nominal angular divergence of $\Delta\theta = 10^{-4}$ radian, electrons are incident over the full length of the 5-meter long jaw.

Additional conditions that can lead to continuous or transient power deposition in the BSY vacuum envelope are (1) misalignment of components which may expose surfaces to the beam which are normally not exposed; (2) mis-steering of the beam; and (3) magnet malfunction or failure.

The vacuum envelope in the BSY is almost entirely made of 300-series stainless steel. Exceptions are (a) the aluminum vacuum chamber between the bending magnet B-2 and protection collimators PC-10 and 30 (for locations, see Fig. 17-1) and (b) the vacuum chambers in the pulsed magnets PM-1 through PM-5, which are ceramic. The low thermal conductivity of the stainless steel, coupled with its medium-Z property (see Table 20-2) does not permit much power deposition before physical damage occurs from excessive thermal stresses or melting.

To illustrate the heating problem in stainless steel, consider the case of a 20-GeV electron beam with 100-kW average beam power and $\sigma_b = 0.3$ cm impinging on a solid block of 300-series stainless steel. At the shower maximum the average power deposited is readily computed from a modified form of Eq. (20-6) to be $P' = 6.9$ kW/cm (using values for iron, which has approximately the same Z and ρ as stainless steel). For a beam PRR of 360 pulses/sec the temperature rise per pulse in stainless steel is then about 7°C as can be seen either from Eqs. (20-5) and (20-6) or from Table 20-2 by proper scaling. At a repetition rate of 360 pulses/sec, the low thermal conductivity of stainless steel does not permit adequate heat diffusion between individual pulses and, hence, the temperature builds up rapidly.

The power loss from a dispersed or mis-steered beam in most places in the BSY is distributed in the horizontal plane along the length of the vacuum chambers in the magnets and interconnecting vacuum pipes. In general, the beam height is small and, thus, the heat generation may be assumed to take place in a line source along the length of a chamber or pipe.

Assuming power deposition on one side of a pipe, the heat flow from the source in the circumferential direction of the pipe may be deduced from the equation of heat flow in a fin which is of finite length and insulated at

its end.[38] The heat transfer per unit length of pipe to the surrounding atmosphere is

$$q' = 2(t\bar{h}k)^{1/2}(T_s - T_\infty)\tanh \pi R\left[\frac{\bar{h}}{(kt)}\right]^{1/2} \tag{20-28a}$$

where

t is the wall thickness of the pipe
$\bar{h}$ is the average coefficient of heat transfer by natural convection and radiation
k is the thermal conductivity of the pipe material
R is the radius of the pipe
T_s is the maximum metal temperature at the source
T_∞ is the ambient temperature of the surrounding atmosphere.

Since the thermal conductivity of stainless steel is low, this equation reduces to

$$q' = 2(t\bar{h}k)^{1/2}(T_s - T_\infty) \tag{20-28b}$$

for all sizes of pipe over 15 cm diameter. If a metal temperature rise over the ambient of $(T_s - T_\infty) = 150°C$ is permitted and if an average heat transfer coefficient of 1.4 W/(cm^2 °C) is assumed, the power deposition along one side of a stainless steel pipe can be only about $P' = 3.7$ W/cm.

In the BSY there are several hundred vacuum couplings which use an indium gasket to make the vacuum seal. Because of the low melting point of indium, an upper limit of 80°C was placed on the local temperature so that the softening and consequent change in the flow properties of the indium would not result in a vacuum leak. With respect to the ambient, this maximum local temperature corresponds to a temperature rise of about $(T_s - T_\infty) \approx$ 50°C. The radial thickness of the vacuum coupling flange is 2.5 cm and thus provides a larger area to conduct heat away from the source in the circumferential direction than does a pipe. However, with the lower limit on the maximum allowed metal temperature, a local power deposition of only about 3 W/cm can be permitted along the coupling.

In a few areas of the BSY it was possible to minimize the potential amount of power deposition by making the vacuum pipes sufficiently large. Space limitations and availability of quick-disconnect vacuum couplings, however, greatly restricted this design. A nominal 30 cm diameter was the largest-sized coupling used in sufficient numbers to be economical to produce.

In most instances, the beam transport components have very limited aperture sizes. Rather small gaps are used in the bending and quadrupole magnets for reasons of economy. The differential pumping system oil trap which divides the accelerator and BSY vacuum systems had to be restricted to a 2.5-cm aperture for functional reasons, but it introduced a constriction in this area. The microwave beam position monitors in the BSY were limited to a 5-cm diameter aperture which could be increased only at the expense of a great loss in sensitivity. Furthermore, any beam power deposition in these

monitors had to be avoided, since a temperature change[34] of more than 5°C can cause the cavity output voltage to vary more than the desired maximum of $\pm 1.5\%$.

Beam trajectory and beam envelope studies

The devices most effective in providing equipment protection in the BSY are the fixed-aperture protection collimators (PC's). These operate by directly intercepting any beam electrons and/or scattered radiation which have the potential for causing damage. Figure 20-21 is typical of the kind of studies that were made to arrive at the proper choice of apertures and of locations for the PC's. In particular, Fig. 20-21 is a study of the beam trajectories between PC-10 and the symmetry quadrupole Q-12, which led to the specification of the aperture sizes and locations of PC-10, 18, and 11 in the A-beam line. (For layout convenience, the 12° bend in the beam was straightened out and, hence, required that the vacuum chambers through the bending magnets B-10, 11, 12, and 13 be shown curved.) These studies also led to the specification of locations for mounting surface temperature sensors on vacuum chambers and for placing ionization chambers. The design beam used in these studies had a radius of 0.3 cm and a divergence of $\Delta\theta = 10^{-4}$ radian at the pulsed switching magnets PM-1 through PM-5. The layout shows that the horizontal width of the aperture through PC-10 was dictated by both the position monitor P-10 and the quadrupole magnet Q-11. The design momentum deviation that PC-10 passes is $\pm 2.65\%$, assuming it is properly aligned, and it intercepts all electrons on the low-energy side between 2.65 and 20.5%.

Figure 20-21 A-beam trajectory study, PC-10 to Q-12.

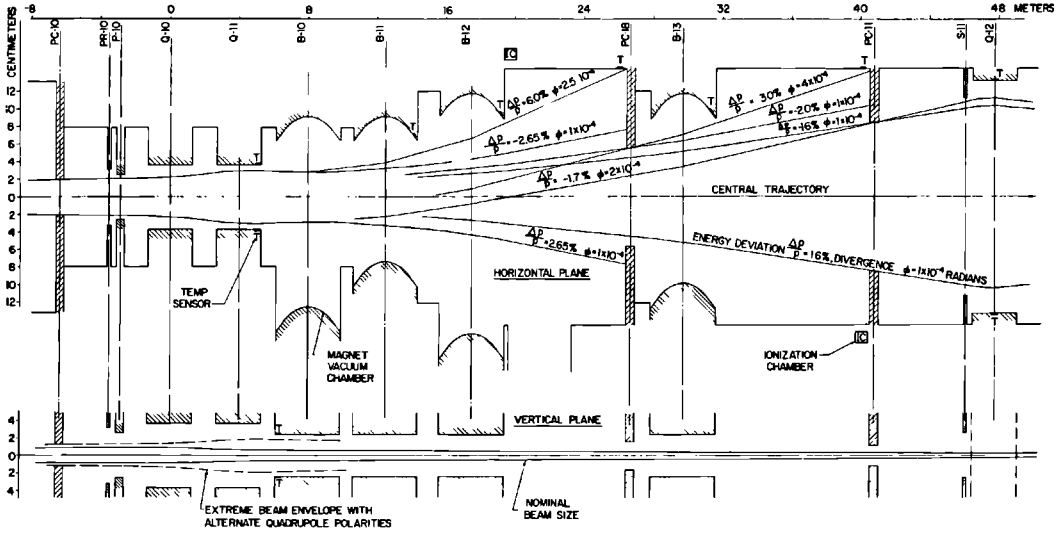

Any lower-energy electrons are incident with a very low power density over the length of the vacuum chamber between the pulsed magnets and PC-10. The electron beam can impinge on the downstream end of the vacuum chamber in Q-11 when there are (1) nonnominal field settings in the quadrupoles (e.g., stronger horizontal defocusing in Q-10) and (2) relative misalignments. Temperature sensors for protection of the vacuum chamber are installed on each side and interlocked to shut off the accelerator if the temperature reaches the trip level.

As the beam passes through the bending magnets B-10 through B-13, it becomes further dispersed. The layout showed that the vacuum chamber in B-13 was quite exposed to power deposition, and, therefore, PC-18 was installed. It passes a momentum deviation of $\pm 2.00\%$. A smaller aperture and resulting transmission of a narrower momentum spectrum would increase the probability of intercepting significantly more power at a very high power density (because of the closeness of the edge of the aperture to the center of the momentum spectrum). It also would make PC-18 more sensitive to transverse misalignments. The PC-11 was installed to protect the quadrupole magnet Q-12 and the instruments located in front of it. It passes a momentum deviation of $\Delta p/p = \pm 1.60\%$ from the design beam. It was located 7 meters upstream from the center of Q-12 in order to eliminate the need to water-cool the vacuum pipe in this area. The pipe size was limited by the largest vacuum coupling size available, i.e., 30 cm diameter. To locate PC-11 further upstream would have made it more sensitive to transverse misalignments, which would result in increased exposure to high power density. Downstream of Q-12, the slits intercept all power arriving outside their aperture but passing through PC-11.

Slight misalignments or bending errors may cause the exit ends of the vacuum chambers in B-11, 12, and 13 to be exposed to small steady power depositions. Therefore, temperature sensors were installed at these locations to detect any abnormal temperature buildup. For the same reasons, temperature sensors were installed near the upstream ends of PC-10, 11, and 18 to protect the indium-sealed vacuum couplings. To guard against any sudden large power depositions due to steering errors or magnet malfunctions, ionization chambers were installed at the exit of B-12 and in front of PC-11.

Because the large bend angles occur only in the horizontal plane, there is no beam dispersion or gross missteering capability to protect against in the vertical plane. Attention was given to effects in the vertical plane caused by possible small missteering or from scattering of electrons caused by insertion of a profile monitor into the beam.

The layout in Fig. 20-21 shows that the vertical aperture in PC-10 was designed to protect the entrance of B-10 when Q-10 and Q-11 are operating opposite to the present polarity (which happens to be the case in the B-beam). Only a small clearance was allowed between the beam and the entrance to the vacuum chamber in B-10 so that the vertical aperture in PC-10 was not unduly reduced. Temperature sensors were installed on the top and bottom

sides of the vacuum chamber to detect any temperature buildup when misalignments permit the beam to reach it. The beam height diminishes in size between B-10 and Q-12 and does not encounter any vertical aperture limitations. However, insertion of the Cerenkov profile monitor PR-10 into the beam causes an increase in the angular divergence due to 2.4×10^{-3} or 6.0×10^{-3} radiation lengths of material through which the beam must pass. The two thicknesses correspond to the use of helium or argon, respectively, in the instrument. The vertical aperture in PC-11 was designed to prevent scattered electrons from reaching and generating heat in the thermally isolated foil supports of the beam energy spectrum monitor S-11. Because of the shape of its aperture, PC-11 also provides protection for the diamond-shaped vacuum chamber of Q-12. In order to observe any temperature buildup from scattered particles or misalignments, temperature sensors were installed at the mid-length of the chamber and in the horizontal plane.

A section of the BSY that was somewhat more difficult to cope with was the region in the A-beam line between the target changer TC-20 and the dump D-11. When a photon beam is required in the end station, a thin target is inserted into the beam at TC-20. The electrons emerging from the target are removed from the photon beam by the dump magnets B-23 through 26. They are bent 12° downward into the window of D-11. The nearly monoenergetic electron beam (maximum momentum deviation $\Delta p/p = \pm 1\%$) which enters the target, however, emerges with a fairly broad momentum spectrum which then is widely dispersed by the dump magnets. Many of these electrons impinge on the dump magnets and on the vacuum pipe following the magnets. For the purpose of engineering the geometry and power absorption capacity of this system, the energy spectrum after the target (to within a few percent of E_0) was assumed to be approximately given by[39]

$$N(E)\,dE = \frac{t\,dE}{E_0 - E} \tag{20-29}$$

for $(E_0 - E)/E_0$ larger than a few percent. $N(E)\,dE$ is the fraction of the total number of electrons in the energy interval dE, E is the energy of an electron emerging from the target, E_0 is the energy of the incident electron beam, assumed to be monoenergetic, and t is the target thickness in radiation lengths. The fraction of the total power in all electrons of which the energy is smaller than E_1 is, then,

$$P = \int_0^{E_1} \frac{t\,dE}{E_0 - E} = t\left[-\frac{E_1}{E_0} - \ln\frac{(E_0 - E_1)}{E_0}\right] \tag{20-30}$$

The dump D-11 was designed with a 15-cm diameter window. The design of the power-absorbing capacity of the system upstream from the dump was predicated on a target having a maximum thickness of 0.01 radiation length for a 2-MW beam (or 0.02 radiation length for a 1-MW beam, etc.). Requiring that the peak of the spectrum enter the dump through the window at a

location 2.5 cm above its geometric center, it was estimated that approximately 83 kW of the dispersed beam would fall outside of the dump window.

Despite the fact that this amount of power is distributed over a fairly large distance (about 30 meters), the local power deposition is too high to depend on the natural convection mode of heat transfer. Lack of space between the magnets made it impossible to use PC's for absorption of all the dispersed beam. Therefore, the bottom sides of the vacuum chambers in the dump magnets B-23 through 26, and the bottom of the drift pipe between B-26 and PC-12 are all water-cooled. The PC-12, having a 10-cm aperture, assures that any beam passing through it will properly pass through the dump window.

The protection system of the entire BSY was developed from geometrical studies similar to the foregoing. Table 20-10 contains a list of the as-built apertures in the water-cooled PC's in the BSY. The various aperture sizes reflect the changing cross-sectional geometry of the beam as it enters and leaves the BSY.

Design features

A total of fourteen PC's were designed to absorb continuously up to 20 kW average power, and a total of six were designed to absorb continuously up to 5 kW. The latter group (PC-3, 4, 5, 7, 8, and 9) protects the ceramic vacuum

Table 20-10 Protection collimator dimensions

Protection collimator No.[a]	*Aperture width (cm)*	*Aperture height (cm)*	*Copper width (cm)*	*Copper height (cm)*	*Aperture length (cm)*	*Average power absorption capacity (kW)*
PC-1	2.077	Circular	20.3	Circular	36.53	20.0
PC-2	2.228	Circular	20.3	Circular	36.53	20.0
PC-3	8.585	2.438	26.0	15.6	32.08	5.0
PC-4	9.911	2.438	26.0	15.6	32.08	5.0
PC-5	11.598	2.438	26.0	15.6	32.08	5.0
PC-6	4.209	Circular	20.3	Circular	36.53	20.0
PC-7, 8, 9	7.038	2.438	26.0	15.6	32.08	5.0
PC-10, 30	3.988	2.479	27.9	17.8	44.91	20.0
PC-11	16.916	2.258	40.6	17.8	44.91	20.0
PC-12, 400[a]	10.173	Circular	29.8	Circular	35.41	20.0
PC-14, 32	8.915	2.248	22.9	17.8	44.91	20.0
PC-15	3.980	Circular	20.3	Circular	36.53	20.0
PC-16	4.623	Circular	20.3	Circular	36.53	20.0
PC-18	11.186	3.200	38.1	17.8	44.91	20.0
PC-31	15.255	2.256	40.6	17.8	44.91	20.0
PC-33	3.820	Circular	20.3	Circular	36.53	20.0

[a] All PC's except PC-400 are shown in Fig. 17-1. PC-400 is located in front of beam dump east.

chambers and the coils in the pulsed magnets (primarily from the scattered radiation emanating from the high-power collimator). Each unit is equipped with two ionization chambers, one mounted above and one below the PC to monitor the power absorbed and to shut off the beam if the power deposition exceeds a preset level. Additionally, platinum resistance-type immersion temperature sensors are installed in the cooling-water supply and return lines. These are also interlocked to shut off the beam should the temperature difference exceed a preset level. In addition to serving as a slow backup to the ionization chambers, the temperature sensors are also used to calibrate them, since the steady-state power deposition can be determined calorimetrically from the water temperature rise. Figure 20-22 shows a typical assembly of a PC with its ionization chambers installed. The quick-disconnect cooling water and vacuum couplings can also be seen.

The ionization chambers respond quickly and roughly proportionally to the amount of power deposition in a PC. Since only a few high-power beam pulses may be sufficient to cause thermal damage, they have a distinct advantage over more slowly responding temperature sensors. Should the entire beam be deposited in a PC, the response time of the electronic circuitry is such that the trip level of the ionization chambers is reached before the next pulse arrives when operating at 360 pulses/sec.

Figure 20-22 Protection collimator with ion chambers.

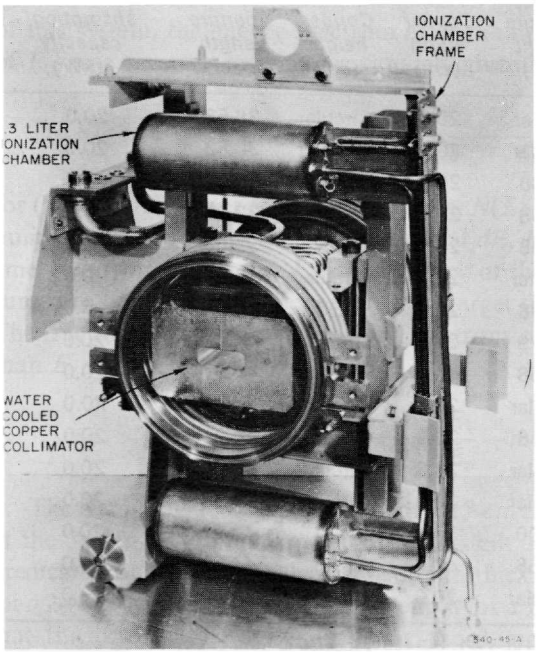

In order to achieve a reasonably compact configuration, it was desirable to mount the ionization chambers as closely as possible to the body of the PC. Because of the close proximity to the radiation source and because the ionization chambers saturate easily, it was necessary to limit the amount of radiation reaching them by shielding. Copper is used as the power-absorbing material in the PC's. Therefore, shielding was most easily accomplished by providing sufficient radial thickness between the region of power deposition and the outside surface of the copper body. For the particular ionization chambers used, this resulted in a radial thickness of approximately 5 radiation lengths or about 7.5 cm between the aperture and the top and bottom surfaces for the 20-kW PC's. The cross-sectional dimensions of the various units are summarized in Table 20-10.

The PC's are a major source of radiation in the BSY. The radial thickness chosen provided sufficient self-shielding to attenuate a large amount of the radiation which would otherwise increase the noise level in the local electronics and accelerate the deterioration of insulation on electrical cables and magnet coils.

The foregoing arguments concerning the specification of the radial thickness of the PC's are also applicable to the specification of the axial length. Since the longitudinal shower development is much more extensive than the radial, the axial length of the copper is correspondingly greater. Furthermore, each one of the microwave position monitors has a PC upstream of it and, therefore, the axial length had to be large enough to minimize the possibility of power deposition in these temperature-sensitive monitors. The length also serves to minimize the radiation deterioration of the ferrite rings in the current intensity monitors, particularly in the monitor I-2; see Fig. 17-1.

In view of the foregoing considerations, the minimum length through the shortest path (i.e., through any cooling-water passages) in the vicinity of the aperture was established as 25 radiation lengths. This is equivalent to 33.5 cm of solid copper. (PC-3, 4, 5, 7, 8, 9 were exceptions because the available space allowed only 24.2 cm of solid copper.) A length of 25 radiation lengths attenuates the power to less than 0.5% of the incident beam power.

The PC's were fabricated in two basic geometries: circular for the units that required a circular aperture and rectangular for those with a rectangular aperture. The circular PC's consist of a 12.5-cm diameter copper core (with the aperture bored through the center) surrounded by a copper sleeve having an outside diameter of 20 cm to satisfy the radial thickness requirement. This core was limited to 12.5 cm diameter so that the cooling-water interface would not be too far from the aperture. For an incident beam of 20 kW average power the longitudinal power deposition at the shower maximum is about 1.65 kW/cm (from Fig. 20-1). Depending on the beam size, the power density can cause metal temperatures in excess of 300°C. The thermal stresses resulting from such a temperature difference exceed the yield strength of copper, and after some cycling may well lead to cracking in the aperture. As long as the cracks do not propagate to the cooling-water interface and admit

water to the vacuum system, the function of the PC's is not impaired. A much lower metal temperature could be realized for the same incident beam power if aluminum were used (see, for example, Table 20-2). However, the radiation length in Al is about 7 times that of Cu and the space requirement for an aluminum protection collimator is far greater than was available. A composite construction was not undertaken for economical reasons, since the PC's are considered to be expendable items.

Fabrication details and materials

As mentioned above, the circular PC's consist of a 12.5-cm diameter copper core surrounded by a copper sleeve. A 1.25 × 1.25-cm cooling-water channel was machined into the outside diameter of the core in the form of a thread with a 2.54 cm (1 in.) lead. Stainless steel, Type 304-L, nipples were inserted into the outside diameter of the sleeve near the ends of the collimator to provide for the cooling-water supply and return lines. Stainless steel, Type 304-L, adaptor rings for welding on the vacuum couplings were added to each end of the core and sleeve assembly. The entire assembly was then brazed together in one operation. PC-12 was fabricated in essentially the same way except that the core was made larger to accommodate the 10-cm diameter aperture. Since the core was also made with a larger radial thickness, stainless steel instead of copper was used for the outer sleeve.

The copper body of the rectangular PC's was made in two halves with the joint running in the axial direction. The rectangular aperture was formed by first machining one-half of the aperture into each piece and then brazing the two halves together. Most of the rectangular PC's are required to absorb power mainly in the horizontal plane. Therefore, twelve 1.58-cm diameter cooling-water holes were drilled vertically through the copper blocks (perpendicular to the beam direction) on each side of the aperture. To form a continuous cooling-water passage between inlet and exit points at the ends, copper elbows and nipples were brazed to the copper bodies on the top and bottom sides such that the flow spirally laced through the external tubes from the holes on one side of the block to those on the other. The brazing of each unit was carried out in two steps, as described below.

Except for the care that had to be exercised in the handling of large pieces of annealed copper, the fabrication of the protection collimators was routine. However, the brazing operation required special care because of the massiveness of the copper pieces and large joint areas involved.

All brazing operations were carried out in a hydrogen atmosphere furnace, and it was, therefore, essential to use certified OFHC copper to prevent embrittlement and blistering. The wrought copper elbows used for the external cooling water passages of the rectangular PC's were the exception, since they are only available as a stock item in phosphorous, deoxidized copper. However, prior to use they were preheated in a hydrogen atmosphere to the brazing temperature to assure that they were oxygen-free.

The OFHC copper was procured in the form of heavily forged shafts and blocks. To ensure that the crystalline structure of the cast billet was completely disintegrated and that the copper structure was completely free of voids and gas, a maximum grain size of 0.150 mm in the interior of the forgings was specified.

The largest copper body was 18 × 40 × 45 cm in size and weighed about 625 lb. The largest surface area to be brazed was in the longitudinal joint which was needed to form the aperture. Its size was 43 × 45 cm minus the height of the aperture. From an experimental test piece it was determined that a surface flatness of 0.005 cm combined with a brazing alloy sheet thickness of 0.01 cm would produce highly reliable joints with full vacuum integrity.

The most essential requirement in selecting the brazing alloys[40] was that they have a melting point in excess of 925°C. Above 925°C, the hydrogen atmosphere in the brazing retort is completely effective in reducing the chromic oxide. The latter remains on the stainless steel parts of the assembly after proper chemical cleaning. The reduced surface assures wetting when the brazing alloy melts. Three alloys were used in the fabrication of the PC's:

Alloy No. 1: 35 Au–62 Cu–3Ni with a liquidus temperature of 1030°C
Alloy No. 2: 35 Au–65 Cu with a liquidus temperature of 1010°C
Alloy No. 3: 50 Au–50 Cu with a liquidus temperature of 970°C

Alloy No. 3 was reserved for reruns to repair any joints that came out of the previous braze with marginal integrity. The melting point of OFHC copper is 1083°C. The PC's having a circular geometry were brazed in one step with alloy No. 2. The PC's with the rectangular geometry were brazed in two steps: in the first step, the longitudinal joint in the copper was brazed with alloy No. 1 and in the second, the stainless steel adaptor flanges and the copper elbows and tubes for the cooling water passage were brazed with alloy No. 2.

The massiveness of the copper bodies in the PC assemblies required heating and cooling cycles in the brazing operation that ranged from 10 to 16 hours depending on the size of the unit. In the heating portion of the cycle (which required about one-third of the time), the temperature rise of various parts of the assembly was monitored with thermocouples so that the brazing alloy at extended thin sections would not melt before that on the massive copper. Because the gold in the gold–copper brazing alloys has an affinity for copper, it will "pick up" copper from the base metal if permitted to remain too long in the liquid state. A small river of alloy can form, drain a joint, and erode the base metal to the extent of cutting through, for example, the thin copper tubes in an assembly. The PC's were allowed to cool to about 100°C before being removed from the sealed retort so that surfaces which were to be subsequently exposed to vacuum would come out oxide-free and bright.

Most stainless steels become sensitized in the temperature range of 500° to 900°C. Sensitization is the result of either carbide precipitation or the formation of a brittle σ phase. Sensitized steels suffer from intergranular corrosion

and are attacked by nitric acid.[41] The low-carbon stainless steels, 0.04% or less carbon, are desirable because they exhibit low carbide precipitation. There are two grades which are commercially available for fabrication: Type 304-L and Type 316-L. Type 304-L was chosen for all stainless steels that must go through the brazing cycle because Type 316-L contains molybdenum, a σ-phase promoter.

Operating experience

To date (July 1967), the protection system as designed and installed has functioned well. Initially all ionization chambers and temperature sensors had their interlock trip levels intentionally set very low. The runs at higher-power levels have, however, already required that some of these trip levels be raised to prevent frequent shutdown of the accelerator, but in no instance have these increases in threshold levels exceeded any design limitations. The system seems to respond particularly well to transient power depositions such as occur from missteering of the beam and sudden increase of beam spectrum width.

The design philosophy of the entire protection system was predicated on a beam power of 2.2 MW. The real test of the effectiveness of the protection system will come when beam power levels significantly above the 240 kW achieved to date are common. The amount of power associated with the off-momentum regions of the spectrum will probably far outweigh all other sources of excessive power deposition which can damage the BSY beam transport system components.

20-9 Future power absorption devices (DRW)

The power absorbers as described in the foregoing sections are designed to satisfy the SLAC requirements for Stage I ($P_{AV} \leq 600$ kW) and Stage II ($P_{AV} \leq 2.2$ MW). In Section 20-1, it has been demonstrated that only low-Z materials can be used as solids to intercept a 2.2-MW beam.

A survey of low-Z metals readily shows that only aluminum and beryllium alloys are useful engineering materials for power absorber applications. The technology of beryllium fabrication, however, is still in its infancy and production costs are high. Moreover, further reduction of Z below that of aluminum combined with an expected future increase of the incident beam energy, requires even longer devices to attenuate adequately the longitudinal cascade shower. The present high-power slit is 5 meters long to satisfy the 30-radiation length criterion for shower attenuation. As stated previously, the slit should have theoretically zero depth and should coincide with the image of the center of the pulsed magnet. Whether or not the long physical length and low Z of the materials have a detrimental effect on the beam in causing slit scattering and halo formation has not yet been investigated.

However, the length combined with the transport system resolution requirements resulted in some rather difficult precision alignment problems and, therefore, high production costs. A further increase in size will jeopardize dimensional stability during operation as a result of unavoidable temperature gradients in the slit and support structures.

The extensive use of water as a primary power absorbant and coolant created new auxiliary problems. Radiolysis and evolution of large amounts of hydrogen, particularly in the high-power beam dumps, demand expensive instrumentation for H_2 detection, including safety interlocks. The handling of the hydrogen mixed with other radioactive gases, and the disposal of large quantities of contaminated water are costly and require the attention of health physics personnel. In short, low-Z power absorbers have many disadvantages, even though they are successfully employed at SLAC at the present time. An advance in the state of the art is needed.

In the design of future accelerators, attention should be focused on improvement of the output by minimizing beam spectrum widths. Next, modifications of existing low-Z designs are needed with emphasis on quick replacement of components which have failed. A small vacuum leak, for example, may render an expensive and complex piece of equipment useless, unless the faulty part can be easily replaced or repaired. The expected increase in induced radioactivity from future high-intensity, high-power machines should be a challenge to the designer of quick-disconnects and remote-handling equipment. Particular emphasis must be given to the problem of minimizing precision alignment time.

Last but not least, the ultimate goal should be the successful employment of high-Z liquid metals as primary beam absorbants and coolants. To name just a few requirements, these liquid metals must be inexpensive, since significant quantities would be needed. They should have a low vapor pressure for application in the beam transport vacuum systems, thus eliminating the need for solid container walls. They should be nonpoisonous and nontoxic. Materials used in the liquid metal loops must be resistant to corrosion and erosion. There may be no liquid metal that satisfies all requirements, but a reasonable compromise probably can be found which would reduce future power absorbers to manageable proportions.

Acknowledgments

The authors would like to express their particular gratitude to D. Coward, E. L. Garwin, Z. Guiragossián, B. de Raad, H. DeStaebler, J. Jurow, E. J. Seppi, R. E. Taylor, and H. A. Weidner for the many valuable suggestions and contributions during the development of the SLAC power absorbers. J. Wagner was the designer and project engineer for the high-power beam dumps. Most of the high-power slit and collimator system was designed by I. Zavialoff and J. Mitchell, and their experience helped greatly to make the program a success. Valuable engineering and design studies were contributed

by L. Cooper to the high-Z collimator program. Under the leadership of A. Eldredge, the SLAC fabrication groups demonstrated a high degree of technical sophistication during the construction phase of the power absorbers. J. Ryan contributed significantly to the development of prototypes and to the experimental programs.

The efforts of the Astronautics Division of General Dynamics/Corvair, San Diego, California in developing the deep-hole drilling technique for the slit modules deserve to be mentioned.

References

1 B. B. Rossi, *High-Energy Particles*, Prentice Hall, New York, 1952.

2 C. D. Zerby and H. S. Moran, "Studies of the Longitudinal Development of High-Energy Electron-Photon Cascade Showers in Copper," Rept. No. ORNL-3329, Oak Ridge National Laboratory, Tennessee (1962).

3 C. D. Zerby and H. S. Moran, "A Monte Carlo Calculation of the Three-Dimensional Development of High-Energy Electron-Photon Cascade Showers," Rept. No. ORNL-TM-422, Oak Ridge National Laboratory, Tennessee (1962).

4 C. D. Zerby and H. S. Moran, "A Collimator Study for a 20-GeV Electron Beam," Rept. No. ORNL-TM-524, Oak Ridge National Laboratory, Tennessee (1963).

5 Z. Guiragossián, "Longitudinal and Radial Distribution of Shower Development in Cu, H_2O, and Al," Rept. No. SLAC-TN-63-85, Stanford Linear Accelerator Center, Stanford University, Stanford, California (1963).

6 Z. Guiragossián, "Peak Power Densities at the Beam Switchyard Collimator and Slits," Rept. No. SLAC-TN-64-16, Stanford Linear Accelerator Center, Stanford University, Stanford, California (1964).

7 H. S. Carslaw and J. C. Jaeger, *Conduction of Heat in Solids*, 2nd Ed., Oxford University Press, London and New York, 1959.

8 D. R. Walz, "Spot Cooling and Heating of Surfaces with High Velocity Impinging Air Jets," Tech. Rept. No. 61, AD 607 727, Department of Mechanical Engineering, Stanford University, Stanford, California (1964).

9 H. A. Johnson, ed., "Lecture Series on Boiling and Two-Phase Flow for Heat Transfer Engineers," University of California, Berkeley, California (1965).

10 J. Jurow, "Boiling Heat Transfer Peak Heat Flux Correlations and References," Rept. No. SLAC-TN-63-84, Stanford Linear Accelerator Center, Stanford University, Stanford, California (1963).

11 C. E. Taylor and J. F. Steinhaus, "High Flux Boiling Heat Transfer from a Flat Plate," Rept. No. UCRL-5414, University of California, Lawrence Radiation Laboratory, Livermore, California (1958).

12 D. R. Walz, J. Jurow, and E. L. Garwin, *IEEE Trans. Nucl. Sci.* **NS-12**, No. 3, 867 (1965).

13 S. Timoshenko, *Strength of Materials*, Vol. 1, p. 66, Van Nostrand, Princeton, New Jersey, 1955.

14 B. A. Boley and J. H. Weiner, *Theory of Thermal Stresses*, Wiley, New York, 1960.

15 J. Jurow, Stanford Linear Accelerator Center, Stanford University, Stanford, California (private communications).

16 L. R. Lucas, "Dump Window Removal Unit Instructions," Rept. No. SLAC-TN-66-43, Stanford Linear Accelerator Center, Stanford University, Stanford, California (1966).

17 D. R. Walz, L. R. Lucas, H. A. Weidner, R. J. Vetterlein, and E. J. Seppi, *IEEE Trans. Nucl. Sci.* **NS-14**, No. 3, 923 (June 1967).

18 A. O. Allen, *The Radiation Chemistry of Water and Aqueous Solutions*, Van Nostrand, Princeton, New Jersey, 1961.

19 A. R. Anderson and E. J. Hart, *J. Phys. Chem.* **66**, 70 (1962).

20 D. K. Nichols, M. T. Simnad, and V. A. J. VanLint, General Atomic Division of General Dynamics, San Diego, California (private communications).

21 H. A. Schwarz, J. P. Losee, and A. O. Allen, *J. Am. Chem. Soc.* **76**, 4693 (1954).

22 H. A. Mahlman and J. W. Boyle, *J. Am. Chem. Soc.* **80**, 773 (1958).

23 J. A. Ghormley and C. J. Hochanadel, *J. Am. Chem. Soc.* **76**, 3351 (1954).

24 D. R. Walz, "Heat Transfer and Thermal Stress Analysis of Slits and Collimators," Rept. No. SLAC-TN-64-29, Stanford Linear Accelerator Center, Stanford University, Stanford, California (1964).

25 L. R. Lucas and D. R. Walz, "Heat Transfer and Thermal Stresses in Tube-Forest Slits and Collimator," Rept. No. SLAC-TN-64-61, Stanford Linear Accelerator Center, Stanford University, Stanford, California (1964).

26 H. DeStaebler, Stanford Linear Accelerator Center, Stanford University, Stanford, California (private communications).

27 G. Rogers, Stanford Linear Accelerator Center, Stanford University, Stanford, California (private communications).

28 S. C. Lind, C. J. Hochanadel, and J. A. Ghormley, *Radiation Chemistry of Gases*, Reinhold, New York, 1961.

29 D. A. G. Neet, "Radiation Exposure in the Switchyard," Rept. No. SLAC-TN-65-9, Stanford Linear Accelerator Center, Stanford University, Stanford, California (1965),

30 D. R. Walz and E. J. Seppi, "Irradiation of Highly Radiation-Resistant Organic Lubricants and a High Temperature Paint," Rept. No. SLAC-TN-67-13, Stanford Linear Accelerator Center, Stanford University, Stanford, California (1967).

31 D. R. Walz, "Corrosion in an Aluminum–Stainless Steel System," Rept. No. SLAC-TN-64-17, Stanford Linear Accelerator Center, Stanford University, Stanford, California (1964).

32 E. Deltombe and M. Pourbaix, *Corrosion* **14**, 496t (1958).

33 U.S. Office of Naval Research, *The Effects of Radiation on Materials* (J. J. Harwood *et al.*, eds.), Reinhold, New York, 1958.

34 D. A. G. Neet, ed., "Instrumentation, Computer Control and Electronic Systems for the SLAC Beam Switchyard," Rept. No. SLAC-68, Stanford Linear Accelerator Center, Stanford University, Stanford, California (1966).

35 E. Rabinowicz, *Friction and Wear of Materials*, Wiley, New York, 1965.

36 D. H. Buckley and R. L. Johnson, "Friction and Wear of Hexagonal Metals and Alloys As Related to Crystal Structure and Lattice Parameters in Vacuum to 10^{-10} Millimeters of Mercury," ASLE Paper No. 65 LC-18, American Society of Lubrication Engineers (1965); Also as Rept. No. NASA-TM-X-52096, National Aeronautics and Space Administration (1965).

37 B. de Raad, "Protection of the BSY Equipment against Overheating by the Electron Beam," Rept. No. SLAC-TN-64-54, Stanford Linear Accelerator Center, Stanford University, Stanford, California (1964).

38 F. Kreith, *Principles of Heat Transfer*, p. 48, International Textbook Co., Scranton, Pensylvania, 1958.

39 B. de Raad, "Beam Profile Monitors for the Beam Switchyard," Rept. No. SLAC-TN-64-77, Stanford Linear Accelerator Center, Stanford University, Stanford, California (1964).

40 H. Soderstrom, Stanford Linear Accelerator Center, Stanford University, Stanford, California (private communication).

41 H. F. Ebling and M. A. Scheil in *Advances in the Technology of Stainless Steels and Related Alloys*, Special Tech. Publ. No. 369, p. 275, ASTM, Philadelphia, Pennsylvania, 1965.